Soft Matter

PERSPECTIVE

View Article Online
View Journal | View Issue

Cite this: *Soft Matter*, 2025, **21**, 3443

Harnessing interfacial entropic effects in polymer grafted nanoparticle composites for tailoring their thermo-mechanical and separation properties

Aparna Swain,†[a] Nimmi Das Anthuparambil,[bc] Nafisa Begam,[d] Sivasurender Chandran *[e] and J. K. Basu *[a]

Nanocomposites based on polymeric materials have been extensively studied to understand and control the thermodynamics, flow, and mechanical properties of the underlying matrix as well to create new materials with diverse optical, electrical, magnetic, separation, catalytic, and biomedical properties. In the form of thin films or membranes, such materials can impart remarkable improvements in various properties of the underlying substrates. Using nanoparticles with grafted polymer chains usually overcomes a major hurdle in achieving enhancements in various properties by enabling better dispersion in the matrix while at the same time introducing a new parameter – interfacial entropy – leading to the emergence of new parameter space for tuning dispersion, flow and thermal properties. In this article, we highlight how this interfacial entropic effect can be harnessed to control various properties in thin films and membranes of grafted nanoparticle composites, in particular their thermo-mechanical properties, viscosity, fragility, glass transition temperature (T_g), and dynamic heterogeneity as well as their ability to act as highly selective gas separation and water desalination membranes. We discuss the application of a range of experimental techniques as well as molecular dynamics simulation to extract these properties and obtain microscopic insight into how the interplay of various surface and interfacial effects lies at the centre of these significant property improvements and enhanced functionality. Finally, we provide an outlook on future opportunities for designing sustainable PNCs, emphasizing their potential in environmental, energy, and biomedical applications, with advanced experiments and modelling driving further innovations.

Received 31st December 2024,
Accepted 29th March 2025

DOI: 10.1039/d4sm01549e

rsc.li/soft-matter-journal

[a] *Department of Physics, Indian Institute of Science Bangalore, 560012, India. E-mail: basu@iisc.ac.in*
[b] *Department of Physics, Universität Siegen, Walter-Flex-Str. 3, 57072 Siegen, Germany*
[c] *Deutsches Elektronen-Synchrotron DESY, Notkestr. 85, 22607 Hamburg, Germany*
[d] *Department of Physics, Institute of Science, Banaras Hindu University, Varanasi, Uttar Pradesh 221005, India*
[e] *Soft and Biological Matter Laboratory, Department of Physics, Indian Institute of Technology, Kanpur-208016, India. E-mail: schandran@iitk.ac.in*
† Current address: Department of Molecular and Cellular Biology, Harvard University, Cambridge, 02138, Massachusetts, USA.

Aparna Swain

Aparna Swain earned her PhD (2022) in physics from the Indian Institute of Science, Bangalore, specializing in the dynamics and transport properties of polymer nanocomposites. She then joined the University of Pennsylvania as a postdoctoral fellow, studying protein–protein phase separation near lipid bilayers and its role in membrane internalization. She is now an incoming postdoctoral research fellow at Harvard University, focusing on the mechanisms of bacterial cell division.

Nimmi Das Anthuparambil

Nimmi Das Anthuparambil received her PhD in physics from the Indian Institute of Science, Bangalore, India, in 2020. Her PhD focused on understanding temperature-dependent structural and dynamical changes in polymer nanocomposites, including bulk materials, thin films, and membranes. Since 2020, she has been a postdoctoral researcher at the University of Siegen, Germany, in collaboration with the Deutsches Elektronen-Synchrotron (DESY), Germany. Her research focuses on polymers (nanocomposites and thin films) and proteins (structure, dynamics, and gelation), utilizing scattering techniques.

1 Introduction

Polymer nanocomposites (PNCs) are multifunctional materials that have been extensively investigated in the last few decades due to their novel thermal, mechanical, electrical, optical and magnetic properties.[1–18] Apart from the various applications in which PNCs have already been found to be useful, from a fundamental science perspective they have provided a platform for exploring rich emergent phenomena in soft matter and materials physics.[19–27] The original motivation for incorporation of nanoparticles in a polymer matrix was to increase the effective interface area between the nanoparticles and the matrix to enhance the desired properties. Here, the assumption was that the nanoparticles are a passive additive and that the total area would simply scale with the particle volume fraction. However, as in other areas of condensed matter physics, the interface turned out to be an independent entity and phase by itself.[28–32] This not only led to unexpected variations in physical properties like giant changes in the viscosity and thermo-mechanical properties[4,33–35] of nanoparticle embedded polymers, but also led to the emergence of a complete phase diagram for the hierarchical self-organization of nanoparticles within polymer matrices.[2,21,36,37]

In PNCs, both entropic and enthalpic effects contribute to their thermomechanical properties and overall performance. While minimizing enthalpic interactions is often desirable for achieving stable dispersion, it is important to recognize that enthalpic effects cannot be entirely disregarded in practical applications.[38–41] Numerous studies and reviews have extensively explored the role of enthalpic interactions in PNCs, including polymer–nanoparticle interactions involving van der Waals forces, hydrogen bonding, and chemical compatibility, which significantly influence their dispersion and phase behaviours.[4,13,42] Given the rich physics and literature on PNCs, covering all the aspects controlling their behavior is beyond the scope of a single review. Thus, to be concise and instructive, in this review, we limit our focus to enthalpically neutral mixtures of polymers and polymer grafted nanoparticles (PGNPs). The phase and dynamic behaviors of such systems are driven by the entropic interactions at the interface of polymers and PGNPs. We highlight how the entropic effects at the polymer–PGNP interface could be harnessed to achieve precise control of the dispersion of particles, and hence, gain a deeper understanding of the underlying mechanisms governing the behavior of PNCs. To this end, we describe how engineering the conformation of the grafted polymers by varying the graft chain length, grafting density or the nanoparticle core size can lead to dramatic

Nafisa Begam

Nafisa Begam pursued her PhD at the Indian Institute of Science, Bangalore, India. Her research focused on investigating thermomechanical properties and dynamics in polymer nanocomposite thin films. Following that, since 2017, she has been working in the field of biophysics as a postdoctoral research fellow at the Institute of Applied Physics, University of Tuebingen, Germany employing X-ray and neutron scattering-based techniques. Her research centered on exploring liquid–liquid phase separation and gelation in protein-based systems. She is currently working as an Assistant Professor at the Department of Physics, Banaras Hindu University, Varanasi, India.

Sivasurender Chandran

Sivasurender Chandran pursued his MSc (2008) in Materials Science at Anna University, Chennai and PhD (2014) in Soft Condensed Matter Physics working with Prof. Jaydeep K Basu at the Indian Institute of Science (IISc), Bengaluru. He had post-doctoral stays at the University of Freiburg (2014–2019), working with Prof. Guenter Reiter, and at the University of Tubingen (up to March 2020), working with Prof. Frank Schreiber. Since 2020, he has been serving at the Department of Physics, IIT Kanpur as an Assistant Professor. His research group focuses on various nonequilibrium phenomena observed in soft and biological matter, including structure formation and dynamics of polymeric materials at various length scales, collective dynamics of bacterial communities, and biofilm formation.

J. K. Basu

Jaydeep K. Basu completed his PhD at the University of Calcutta (2000) followed by postdoctoral stints at the University of Illinois, Urbana-Champaign, Argonne National Laboratory and CEA, Saclay/U Paris-Sud. He joined the Department of Physics, Indian Institute of Science (2003), where he is currently the Department Chair and also MSIL Chair Professor. He is a fellow of the Indian Academy of Sciences, Bangalore. His areas of interest range from soft matter, the physics of biological systems, super-resolution optical microscopy, synchrotron and neutron scattering, and spectroscopy to quantum photonics and quantum information processing.

changes in various properties of either PGNP assemblies or membranes and in PNCs made of polymers embedded with such grafted nanoparticles. In addition to the usual parameters mentioned above, an additional parameter has been introduced, which we use as an effective representation of the entropic interaction effect, f, between the grafted and matrix chains. We will delineate the role of f in controlling the dispersion of PGNPs in polymer matrices, thereby controlling the thermomechanical properties of PNCs and their performance in membrane technologies, such as water desalination and gas separation.

To establish a clear understanding of the entropic effects in polymer–PGNP systems, we begin by highlighting what we mean by interfacial entropy and how f allows controlling it. Upon mixing chemically identical matrices and graft polymers, deviations in the conformational entropy at the particle–polymer interface due to the stretching of graft/matrix polymers facilitate phase separation/homogeneous mixing. This conformational entropy of polymer chains at the particle–polymer interface is what we refer to as interfacial entropy. Grafting the nanoparticles with polymers allows harnessing the interfacial entropy *via* the particle size, grafting density, the molecular weight of matrix and grafting chains.[43–48] In particular, the ratio of grafting molecular weight to the matrix molecular weight, defined as f, plays an important role. At a given grafting density, for systems with $f > 1$, the short matrix chains could mix without significant stretching of grafting polymers. This interpenetration between the grafted and matrix polymers results in a broad particle–polymer interface for $f > 1$, and hence, displays a homogeneous dispersion of particles.[43] On the other hand, for systems with $f < 1$, the entropic penalty to accommodate long chains will be significantly larger, which, in turn, results in a sharp interface with reduced monomer density at the particle–polymer interface.[43] This manifests into local or macroscopic phase separation. Naturally, interfacial entropy plays a crucial role in determining not only the dispersion behavior, but also the physical characteristics and hence the functionality of the PNCs.[44,49]

We organize this review as follows: we begin with a brief discussion of the technical aspects of the experimental methods and molecular dynamic simulations discussed in this article. Subsequently, we delineate the role of conformation of grafted chains in controlling the interfacial entropic effects and, hence, in tuning the dispersion of PGNPs in polymer matrices. Afterwards, we will highlight how interfacial entropic effects can be utilized to tune various thermo-mechanical properties such as the glass transition temperature, viscosity and fragility of PGNP based PNCs (bulk and thin films) and membranes. In particular, when PNCs are confined such as in thin films or thin coatings, we will emphasize the interplay of two interfaces: (i) the PGNP–matrix polymer interface, characterized by the thickness of the graft–matrix chain inter-mixed region ξ, and (ii) the substrate–film interface, defined by the thickness of the adsorbed layer h_{int}. Furthermore, we discuss in detail how entropic coupling between graft and matrix chains can be tuned to create dispersed PNCs with high NP loading and membranes for gas and water separation. We conclude by outlining the prospects for creating sustainable PNCs, highlighting their potential for use in energy, biomedicine, and environmental applications.

2 Methodologies: experimental and computational approaches

2.1 Preparation of PGNPs

Polymer grafted nanoparticles, nanoparticles (often inorganic) grafted with long polymer chains, are a class of soft nanocolloidal systems with versatile properties. Grafting inorganic nanoparticles (NPs) with polymers, in addition to providing stabilization against aggregation, provides new levers to control the dispersion of the nanoparticles in polymer matrices. In this section, we briefly review the two methods – grafting-from[50–52] and grafting-to[53–61] – that are predominantly used for the synthesis of PGNPs. The grafting-from method involves growing polymer chains directly from nanoparticles by attaching initiators to their surface and polymerizing monomers.[62] This approach allows for high grafting density and precise control of chain lengths but often results in higher polydispersity compared to the grafting-to method. Techniques like atom transfer radical polymerization (ATRP), reversible addition–fragmentation chain transfer polymerization (RAFT),[20] or ring-opening polymerization (ROP) are commonly used for controlled polymerization. While the process can be complex, it ensures strong polymer–nanoparticle bonding and is ideal for applications requiring dense, stable polymer coatings.[63,64] In contrast, the grafting-to approach involves attaching pre-synthesized polymer chains to the surface of nanoparticles. Thus, the grafting-to method typically results in a lower polydispersity of grafted chains compared to the grafting-from method. In this report, we focus broadly on studies investigating PGNPs synthesized using the grafting-to method. However, the physics underlying their phase and dynamic behaviors do not depend on their method of preparation.

2.2 Advanced scattering techniques

2.2.1 X-ray reflectivity: probing dispersion of PGNPs along the film thickness. X-ray reflectivity (XR) is a non-destructive technique allowing to probe the electron density gradient or modulations (inhomogeneities) along the film thickness. Thus, XR complements the imaging techniques like transmission (and scanning) electron microscopy, by providing insights into the dispersion of particles along the film thickness. Here, we provide a brief overview of the theory underlying the XR and how roughness, film thickness and density modulations affect the reflectivity profile. For a detailed review of the applications of X-ray reflectivity, the readers may refer to the excellent monographs on this subject.[65,66]

Following Fresnel's theory of reflection, the reflected intensity of X-rays from a surface follows

$$R(q_z) = |\mathrm{SA}|^2 = \left|\frac{q_z - \sqrt{q_z^2 - q_c^2}}{q_z + \sqrt{q_z^2 - q_c^2}}\right|^2 \quad (1)$$

where SA is the scattering amplitude, the momentum transfer $\vec{q}_z = \vec{k}_f - \vec{k}_i$ ($\vec{k}_i$ and $\vec{k}_f$ being the incoming and outgoing wavevectors, respectively) is along the surface normal (z coordinate) and q_c is the critical wave vector. Rephrasing Bragg's law of diffraction, q_z follows

$$q_z = \frac{4\pi}{\lambda}\sin(\alpha_i) \tag{2}$$

where λ is the wavelength of the X-rays. Below a critical wave vector, $q_z < q_c$, there will be a total external reflection. At large scattering angles ($q_z \geq 3q_c$), the reflected intensity takes an asymptotic form given by

$$R(q_z) = \frac{{q_c}^4}{12{q_z}^4} \tag{3}$$

In summary, any representative reflectivity profile will exhibit (a) a plateau, due to total external reflection, at $q_z < q_c$, (b) a steep decrease for $q_z > q_c$, and (c) an asymptotic decay $\propto {q_c}^{-4}$ at large q_z. In addition, the reflected intensity of a rough surface, with roughness δh, falls off exponentially following,

$$R(q_z)_{real} = R(q_z)_{ideal} e^{-2{q_z}^2\delta h^2} \tag{4}$$

On shining X-rays on a film (containing one or more layers) coated on a substrate or floating on a water surface, beyond a critical wave vector q_c, rays get reflected from the top and the bottom surface resulting in periodic oscillations called the Kiessig fringes. At $q_z > q_c$, such oscillations ride on the decrease of R with q_z following eqn (3). The amplitude of these oscillations scales with the electron density contrast of the layer and the interfaces (air–surface and substrate). In addition, the amplitude of such oscillations also decreases with the roughness of the surface following eqn (4).

Paratt's recursion formalism is used to model the reflection and transmission from all j interfaces. This relates the reflected amplitude R_j and transmitted amplitudes T_j at all j interfaces *via*

$$X_j = \frac{R_j}{T_j} = e^{-2iq_{z,j}z_j}\frac{SA_{j,j+1} + X_{j+1}e^{2iq_{z,j}z_j}}{1 + SA_{j,j+1}X_{j+1}e^{2iq_{z,j}z_j}} \tag{5}$$

where the Fresnel reflection of the jth interface follows

$$SA_{j,j+1} = \frac{q_{z,j} - q'_{z,j+1}}{q_{z,j} + q'_{z,j+1}} \tag{6}$$

Using Born approximation, we could relate the reflectivity profile with the thickness dependent electron density $\rho_e(z)$ as

$$R(q_z) = \frac{(4\pi\rho_0 r_e)^2}{{q_z}^4}\int\left|\frac{1}{\rho_0}\frac{d\rho_e}{dz}e^{iq_z z}dz\right|^2 \tag{7}$$

where r_e is Thomson's electron radius and ρ_0 is the mean electron density of the multilayer. This formalism does not include multiple scattering events, prominent at low scattering angles *i.e.* $q \leq q_c$. However, eqn (7) equation is a good approximation for the asymptotic dependence (at $q > q_c$) of the reflectivity profile. In addition, this form nicely underlines that a detailed modelling of the experimental reflectivity profile would allow us to measure the electron density gradient along the film thickness. Thus, modeling of the XR profile allows capturing the dispersion of PGNPs along the film thickness.

2.2.2 Probing the length-scale dependent dynamics

2.2.2.1 X-ray photon correlation spectroscopy. X-ray photon correlation spectroscopy (XPCS) is broadly being used to study dynamics in various hard and soft matter systems by utilizing coherent X-rays from third-generation synchrotron sources[65,67,68] and X-ray free electron laser facilities.[69] Coherent X-ray scattering experiments can explore a variety of phenomena at longer time scales, which is beyond the scope of neutron scattering experiments, and shorter time scales, which are not reached by normal light scattering experiments. The poor spatiotemporal coherence in lab X-ray sources is a limiting challenge. However, the emergence of powerful X-rays from third-generation synchrotron sources provides great opportunities to perform coherent X-ray scattering experiments. XPCS is an X-ray equivalent of dynamic light scattering (DLS). In XPCS, speckle patterns originating from the disorder in the systems are collected at intervals of δt. The time correlation of these speckles provides information about the dynamics of scatters in the system.[70–73] Time correlation of intensity at (q_x, 0) to a later time (q_x, δt) follows,

$$g_2(q_x, \delta t) = \frac{\langle I_p(q_x, 0)\rangle\langle I_p(q_x, \delta t)\rangle}{\left|I_p(q_x, 0)\right|^2}, \tag{8}$$

where I_p is the intensity at pixel p and $\langle\cdots\rangle$ denotes the average over pixels in a q_x-range, where $I_p(q_x, 0)$ is the intensity at wave vector q_x and time $t = 0$. For equilibrium dynamics, using Siegert's relation, we could relate the intermediate scattering function (ISF), $F_s(q_x, \delta t)$, with $g_2(q_x, \delta t)$ by the following relation,[72]

$$g_2(q_x, \delta t) = 1 + b|F_s(q_x, \delta t)|^2 \tag{9}$$

where b is an instrumental factor called the speckle contrast and δt is the delay time. $F_s(q_x, \delta t)$ has the general time dependent functional form,

$$F_s(q_x, \delta t) = \exp[-(\delta t/\tau)^\beta], \tag{10}$$

where τ and β are the relaxation time and Kohlrausch–Williams–Watts (KWW) exponent, respectively. Here, β determines the shape of the correlation function and provides information about the nature of the dynamics. An exponential decay ($\beta = 1$) indicates diffusive dynamics, whereas stretched ($\beta < 1$) exponential decays characterize heterogeneous dynamics.[71] The compressed ($\beta > 1$) exponential decays are typically found in arrested and/or non-equilibrium systems such as gels, foams, and glasses.

2.2.2.2 Quasi-elastic neutron scattering. Quasi-elastic neutron scattering (QENS) is a versatile technique used to probe atomic and molecular dynamics in various systems like liquids, polymers, and biological macromolecules.[74–78] In comparison to other scattering techniques, QENS requires fine energy resolution in the milli-electron volt range. By detecting small energy changes through neutron sources (reactors or spallation

sources) and instruments like time-of-flight or backscattering spectrometers, QENS provides insights into microscopic motion over a broad momentum transfer range.[79]

The differential scattering cross-section is expressed as:

$$\frac{d^2A_s}{d\Omega dE} = \frac{k_f}{k_i}S(q,\omega) \quad (11)$$

where A_s is the scattering cross-section, Ω is the solid angle, E is the energy transfer, and $S(q, \omega)$ is the dynamic structure factor representing system dynamics.[80] For segmental diffusion, $S(q, \omega)$ is modeled by a Lorentzian function:

$$S(q,\omega) = \frac{A(q)}{\pi}\frac{\Gamma(q)}{\omega^2 + \Gamma(q)^2}, \quad (12)$$

where $\Gamma(q)$, the half-width at half-maximum (HWHM), depends on the diffusion coefficient D, segmental jump length l, and characteristic time τ:

$$\Gamma(q) = Dq^2 + \tau^{-1}(1 - e^{-q^2l^2/6}). \quad (13)$$

The intermediate scattering function $F_{is}(q, t)$, derived from the Fourier transform of $S(q, \omega)$, describes time-dependent molecular displacements:[81]

$$F_{is}(q,t) = \int_{-\infty}^{\infty} S(q,\omega)e^{i\omega t}d\omega. \quad (14)$$

For simple Brownian motion, $F_{is}(q, t)$ decays exponentially:

$$F_{is}(q, t) = A(q)e^{-\Gamma(q)t}, \quad (15)$$

where $\Gamma(q) = Dq^2$. In complex systems, a stretched exponential form is used:

$$F_{is}(q, t) = A(q)e^{-(t/\tau(q))^{\beta}}, \quad (16)$$

where the extent of stretching is defined by β ($0 < \beta \leq 1$). A smaller value of β suggests a larger distribution of relaxation times.

QENS uniquely reveals time and spatial scales of segmental motion, making it indispensable for studying diffusion in polymers, glass transition, and constrained dynamics in complex systems.[61,79,81] Through $\Gamma(q)$ and $F_{is}(q, t)$, parameters like diffusion coefficients, relaxation times, and motion length scales are obtained, providing critical insights into materials' properties and molecular interactions.

2.3 AFM for probing viscoelastic properties

Atomic force microscopy (AFM) is a powerful technique, not only for imaging at the nanoscale, but also for probing the viscoelastic properties of materials at the nanoscale.[82,83] AFM uses a sharp tip on a cantilever to interact with a sample surface, allowing to measure properties like stiffness and elasticity with high spatial resolution.[84,85] This is especially useful for heterogeneous materials, such as polymers, biological tissues, and soft matter, where these properties can vary significantly over small length scales.[86] Since conventional rheological techniques will not be reliable for measuring nanoscopic thin films, in Swain *et al.*,[87] we extend the ability of this technique to estimate thin film viscosity using standard force–distance spectroscopy.[88,89] Here, we provide a brief on the physics underlying the method.

Typically, a force–distance curve characterizes the deflection of an AFM tip as it interacts with a sample during the approach (trace) and withdrawal (retrace) phases.[88,89] In the non-contact regime, where the tip is far from the surface, no interaction forces are observed. As the tip approaches the sample, long-range attractive forces, predominantly van der Waals interactions, induce a sudden deflection toward the surface, a phenomenon termed jump-to-contact. Upon further indentation, short-range repulsive forces dominate, leading to cantilever bending, indicative of contact mode AFM imaging. During the retrace phase, the tip is withdrawn from the sample, experiencing adhesive, capillary and viscous forces. The tip detaches from the surface only when the elastic restoring force of the cantilever surpasses these attractive interactions, resulting in a sudden release known as jump-off-contact. Quantitative parameters such as tip-sample adhesion force, total contact force, and pull-off force can be directly extracted from force–distance spectroscopy measurements. The force experienced by the cantilever, when retracted from a viscous surface, is mainly a combination of viscous, F_{vis}, and capillary forces, F_{cap}.[90] Thus, the pull-off force profile of force–distance retrace curves is modeled using the equation

$$F_{AFM}(L) = F_0 + F_{cap}(L) + F_{vis}(L) \quad (17)$$

where F_0 is a constant. Based on the assumption of a finite cylindrical-shaped liquid bridge formed between two spheres (considering the film surface as a sphere of infinitely large radius), F_{vis} is given by ref. 91

$$F_{vis}(L) = -\frac{6\pi {R_{tip}}^2\eta}{L}\frac{dL}{dt} \quad (18)$$

where R_{tip} is the radius of the tip, L is the distance between the tip and the surface of the sample, and $\frac{dL}{dt}$ is the retracting rate of the tip from the sample. On the other hand, F_{cap} is given by

$$F_{cap}(L) = -6\pi R_{tip}\gamma\cos(\theta_c)\left[1 - \frac{1}{\sqrt{1 + \frac{2V}{\pi R_{tip}L^2}}}\right] \quad (19)$$

where γ is the surface tension of the sample, θ_c is the contact angle between the tip and the sample, and V is the volume of the liquid bridge.

In fitting the obtained force–distance curves with eqn (17) the value of dL/dt was kept fixed, as was used in experiments, while all the remaining parameters were varied during the fitting of the data. To eliminate the possible uncertainties resulting from the mutual dependency of R_{tip} and η (refer to eqn (19)), we estimated the temperature-dependent R_{tip} values using reported η values of bulk PS of molecular weight 19 kDa.[92–94] We fitted the force–distance curves obtained for the bare PS films. However, constrained fitting, where both R_{tip} and η are varied, also led to similar results. We have used two offset parameters named x_0 and b_0. Therefore, the force–distance

curves are modeled using the equation given as:

$$F_{\mathrm{AFM}}(L) = F_0 - \frac{6\pi\eta {R_{\mathrm{tip}}}^2}{(L - x_0)}\frac{\mathrm{d}L}{\mathrm{d}t} - 6\pi R_{\mathrm{tip}}\gamma\cos\theta_{\mathrm{c}}\left[1 - \frac{1}{\sqrt{1 + \frac{2V}{\pi R_{\mathrm{tip}}(L - b_0)^2}}}\right] \quad (20)$$

For comprehensive information regarding the fitting of the retrace curve within the force–distance data and the extraction of viscosity, please refer the work of Swain *et al.*[87]

2.4 Coarse grained molecular dynamics simulations

Computer simulations are beneficial for validating the experimental findings and providing more insights into a parameter space that is challenging to access experimentally. The coarse-grained molecular dynamics (CGMD) simulations have been widely used to model polymers and polymer-grafted nanoparticles. Several tools like LAMMPS (large-scale atomic/molecular massively parallel simulator), GROMACS, NAMD, HOOMD-blue, and dissipative particle dynamics (DPD) can be used to perform CGMD simulations. However, the LAMMPS package is often used to perform CGMD simulations due to superior scalability, customizability, and support for polymeric and reactive CG models. In this review, we discuss CGMD simulations on PNCs and membranes performed using the LAMMPS package.[58,60,70,95] A pure polymer system is modeled using linear chains created using a bead-spring model with a hybrid potential of finite extensible nonlinear elastic (FENE) potential and harmonic potential with standard values of the parameters. The linear-chain-grafted nanoparticles were used as a model for PGNPs. All the species of the system interact through the shifted Lennard-Jones potential with the following form

$$E = 4\varepsilon\left[\left(\frac{r_0}{r}\right)^{12} + \left(\frac{r_0}{r}\right)^{6}\right] - E_{\mathrm{rc}} \quad (21)$$

where ε is the reduced energy unit, and E_{rc} is the energy cutoff at $r = r_{\mathrm{c}}$, with r_{c} (in units of r_0) = $(D_1 + D_2)/2$, where D_1 and D_2 the diameters of the interacting species. Basically, the Hamiltonian equations of motion of all species are solved in this method to obtain their position and momentum, interacting *via* the interaction energy described above.

To model a PGNP membrane on the polymer substrate film, we use a bilayer system consisting of a single-layer of grafted nanoparticles atop bulk-free linear chains inside a rectangular box.[58,60] The non-bonded graft–graft monomer interactions were modeled using eqn (21) with $\varepsilon = 1.0kT$, where k is the Boltzmann constant and T the temperature. To model the PGNP/PS system, non-bonded matrix–matrix and graft–matrix interactions were set as the Lennard-Jones potential with $\varepsilon = 1.0kT$ and $\varepsilon = 1.03kT$, respectively.

2.5 Transport through desalination membranes

The solution–diffusion model explains membrane separation as a three-stage process.[96–99] Molecules absorb into the membrane on the feed side, driven by chemical potential gradients and governed by solubility. They then diffuse through the membrane, where their rate depends on the molecular size and compatibility with the polymer, favoring smaller or more soluble molecules. Finally, molecules desorb on the permeate side, completing the transport. This process enables selective separation by leveraging differences in diffusion and solubility, making the model effective for gas separation, reverse osmosis, and pervaporation. However, it assumes ideal transport and may require adjustments for complex mixtures or swelling effects.

The transmembrane flux J, representing either water flux (J_{w}) or salt flux (J_{s}), is determined by the following equation:

$$J = \frac{V}{A_{\mathrm{m}} \times t} \quad (22)$$

where J is the transmembrane flux, expressed in [L m^{-2} h^{-1}] and V is the volume of the permeate (V_{p} corresponds to water and V_{s} corresponds to salt). The effective membrane area is given as A_{m} (= 2.44 cm^2 in our experiments) and t represents the duration of the permeation process. This equation quantifies the transport of water or salt across the membrane per unit area over a specified time period.

Here, V_{s} is determined using the following equation:

$$V_{\mathrm{s}} = \frac{V_{\mathrm{p}} \times C_{\mathrm{p}}}{\rho_{\mathrm{salt}}}. \quad (23)$$

where C_{p} is the concentration of the permeate, and ρ_{salt} is the density of the salt (2.17 g cm^{-3}) on the downstream side.

The salt rejection R_{s} is determined using

$$R_{\mathrm{s}} = \left(1 - \frac{C_{\mathrm{p}}}{C_{\mathrm{f}}}\right) \times 100 \quad (24)$$

where C_{p} and C_{f} are the salinity of the permeate and feed solutions.

The water permeance A (in units of [L m^2 h^{-1} bar^{-1}]) and the salt permeability B (in units of [L m^2 h^{-1}]) are both determined from the relations between flux and permeance as

$$J_{\mathrm{w}} = A(\Delta P - \Delta\pi) \Rightarrow A = \frac{J_{\mathrm{w}}}{(\Delta P - \Delta\pi)} \quad (25)$$

$$J_{\mathrm{s}} = B\Delta C \Rightarrow B = \frac{J_{\mathrm{s}}}{\Delta C} \quad (26)$$

Here, ΔP is the applied pressure on the membrane during the flux experiment, ΔC is the difference between C_{f} and C_{p}, and $\Delta\pi$ is the osmotic pressure difference where the osmotic pressure π is defined as $\pi = iMRT$. Here, i is the van't Hoff factor, M is the molarity of solution, R is the ideal gas constant and T is the absolute temperature. Finally, we determine the water perm selectivity of the membrane as A/B.

To summarize, thus far, we have highlighted a palette of experimental and simulation methods allowing access to the

structural information, microscopic (length-scale dependent) dynamics and macroscopic properties of PNCs. Building on this understanding, in the next section, we describe how the interfacial entropy at the polymer particle interface plays a crucial role in describing the structure and dynamical aspects of PGNPs and their mixtures with polymers.

3 Conformation of grafted chains in PGNPs

Grafting chains on inorganic nanoparticles (see Fig. 1a) provides two important advantages: the presence of an inorganic core provides an avenue to harness several physical properties, and the polymers grafted to the core nanoparticles allow controlling the interactions between them.[1,100,101] As discussed in Section 2.1, several methods were developed to synthesize them either *via* grafted to or grafting from approaches.[3,50–52,54–61,102] The morphology and interactions between PGNPs manifest several parameters including van der Waals interaction between the neighbouring nanoparticles, the enthalpic interaction between the core and the grafted polymers, the molecular weight of the grafting polymers, the grafting density and the quality of the solvent in which the particles are dispersed.[52,103–106] Often, the core size of PGNPs is much smaller than the overall size of the particles. Thus, the contribution of the inorganic core nanoparticles to the interparticle interactions could be neglected. In such a limit, the radial monomer density profile, and hence, the interactions of PGNPs can be approximated with the star polymers.[6,103] In an attempt to build an intuitive background, we begin with a brief discussion on their structural analogues called star polymers, which lack the inorganic core (Fig. 1b).[107–109] We guide curious readers to the focused reviews of star polymers.[107,109–114] Here, we provide a brief discussion of highlighting the parallels between star polymers and PGNPs.

A star polymer contains many polymer arms connected to its microscopic core. It is now well known that the physical behaviour and the interactions between the star polymers reflect the number of arms n_a connected to the core.[113,114,116] Star polymers with low n_a have a uniform distribution of monomers from the surface. On the other hand, star polymers with large n_a possess a close packing of polymers on the surface, resulting in strong steric repulsion between the polymers, which, in turn, leads to a strong stretching of polymers near the core. It is easy to conceive that the volume available per chains increases as we go radially outward. As a result, the extent of stretching of chains decreases with an increase in the radial distance from the core surface. Reflecting such transitions in polymer conformation along the radius, it is convenient to separate a star polymer into three regions: the core, the stretched region near the surface, and the unswollen region at

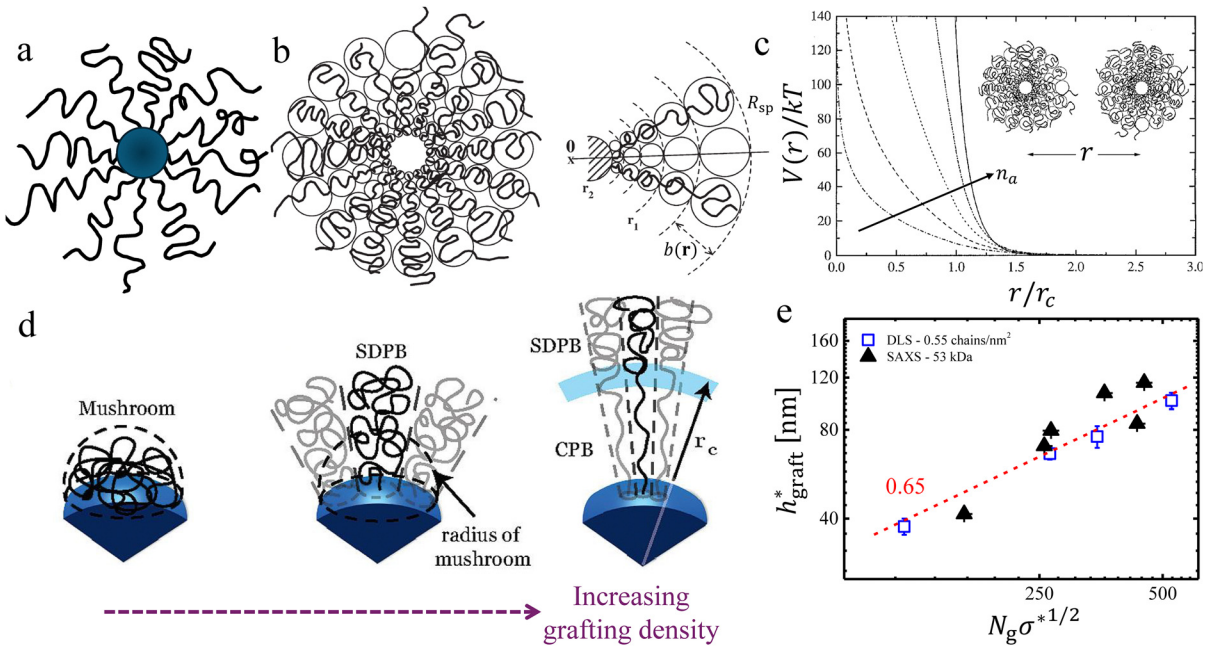

Fig. 1 Conformational transitions – equivalence between PGNPs and star polymers: (a) schematic of a polymer grafted nanoparticle, where the grafted polymers are shown in black lines and the inorganic core nanoparticles are shown as blue spheres. (b) Schematic of a star polymer, shown with blobs for highlighting the conformational transitions radially outward. (c) Effective interaction $V(r)$, normalized with the thermal energy kT, is shown for star polymers with a different number of arms, denoted by n_a. Similar conformational transitions in PGNPs, dictated by the grafting density σ, are shown schematically in (d). The rescaled thickness of the grafted layer h^*_{graft} of the melt graft layer thicknesses, obtained *via* SAXS measurements, and of the thickness in solutions, obtained *via* DLS measurements, are shown. Please refer to the text for discussion on rescaling. The schematic shown in (b) and the plots shown in (c) are adapted from Likos and co-workers,[107,108] and the schematic in (d) is adapted from Dukes *et al.*[48] Data in (e) are extracted from ref. 48 and 115.

the edge. The effective size, quantified by radius R_{sp}, is effectively the sum of three contributions: the radius of the core R_{core}, the length $l_{swollen}$ of the swollen/stretched region, and the length $l_{unswollen}$ of the unswollen region at the edge. The n_a dependence of R_{sp} is nicely captured by the blob model of Daoud and Cotton.[117] In this model, a star polymer is regarded as a succession of concentric shells of blobs, each blob in the shell having size $b(r)$. The radial variation in monomer concentration $c(r)$ and the overall size of the star polymer depends on (a) the solvent quality, which determines the excluded volume parameter v of the chain, (b) the degree of polymerization N and (c) the number of polymers connected to the core also known as the functionality n_a. Using a simplifying assumption that the concentration $c(r)$ of monomers vanishes beyond the radius R_{sp} of the star polymer, the conservation of the number of monomers yields[109]

$$4\pi\int_0^{R_{sp}} r^2 c(r)\mathrm{d}r = Nn_a \tag{27}$$

Using this conservation form and accounting for the different extents of stretching along the radial direction, the radius R_{sp} follows[109]

$$R_{sp} \sim \left[Nn_a + \frac{1}{10}\frac{{n_a}^{3/2}}{\bar{v}^2} + \frac{1}{6}{n_a}^{3/2}\right]^{3/5} \bar{v}^{1/5} {n_a}^{-2/5} a \tag{28}$$

This form of the radius manifests the radial distance-dependent concentration $c(r)$, shown in Fig. 1b. The $c(r)$ and R_{sp} provide an interesting form of the potential,[109]

$$\frac{V(r)}{kT} = \begin{cases} \frac{5}{18}{n_a}^{3/2}\left[-\ln\left(\frac{r}{r_c}\right) + \frac{1}{1+\sqrt{n_a}/2}\right] & \text{for } r \le r_c \\ \frac{5}{18}{n_a}^{3/2}\frac{1}{1+\sqrt{n_a}/2}\left(\frac{r_c}{r}\right)\exp\left(-\frac{\sqrt{n_a}(r-r_c)}{2r_c}\right) & \text{for } r \ge r_c \end{cases} \tag{29}$$

With an increase in n_a, we could observe a systematic increase in the stiffness of the repulsive interactions from ultra-soft to hard sphere like potential (refer to Fig. 1(c)). Inspired by these models, theories were developed to understand the conformational changes of polymers grafted to a nanoparticle.

Qualitatively, the conformations of grafted polymers vary with grafting density σ in a manner similar to the n_a dependence in star polymers (see Fig. 1d). Let us define a reduced grafting density $\sigma^* = \sigma \cdot a^2$, with a being the monomer size. When the grafting density satisfies $\sigma^* < {R_g}^{-3}$, where R_g is the radius of gyration, the grafted polymers display a swollen behavior and this type of conformation is called mushroom conformation. With further increase in σ^*, grafted polymers reveal various conformations from mushroom-like to semi-dilute polymer brush (SDPB) and subsequently to concentrated polymer brush (CPB). Especially, at large σ^*, grafted polymers stretch progressively as we go towards the center of the particle revealing transitions from SDPB to CPB. Extending the ideas of the Daoud–Cotton model, Dukes *et al.* showed that the thickness of the graft layer follows[48]

$$h_{graft} \sim \begin{cases} {N_g}^{3/5} & \text{for mushroom} \\ \left(N_g\sigma^{*1/3}\right)^{3/5} & \text{for SDPB} \\ \left(N_g\sigma^{*1/2}\right)^{x} 3/5 < x \le 1 & \text{for CPB} \end{cases} \tag{30}$$

where N_g is the number of monomers in a grafted polymer. We note that the direct measurements of the conformations of graft polymers are challenging and may require a combination of neutron scattering experiments and rich chemistry (see ref. 118 for measurements on flat brushes). However, changes in the molecular conformations of grafted polymers manifest in differences in the thickness h_{graft} of the graft layer, which is easily accessible. As an illustrative example, in Fig. 1e, we summarize the brush thicknesses h_{brush}^{SAXS} and h_{brush}^{DLS} obtained respectively from small angle X-ray scattering (SAXS) experiments on melts[115] and dynamic light scattering (DLS)[119] experiments on dilute PGNP solutions. For clarity, we rescaled the h_{brush}^{DLS} by an arbitrary factor s_h to obtain $h_{brush}^{*} \approx s_h \cdot h_{brush}^{SAXS} \approx h_{brush}^{DLS}$. Here, DLS experiments were performed on PGNPs with σ = 0.55 chains per nm^2 but with different molecular weights M_g of grafted chains, while SAXS experiments were performed on PGNP melts with M_g = 53 kDa but with different σ values. Inspired by the work of Dukes *et al.*,[48,119] we scaled σ^* with the number of grafted monomers N_g of the grafted chains. We observe that $h_{graft}^{*} \sim \left(N_g\sigma^{*1/2}\right)^{0.65}$. Following eqn (30), this dependence reveals that the grafted chains are in the CPB regime. The conformation of grafted chains plays a crucial role in deciding the dispersion behavior of PGNPs in polymer matrices. We will focus on this aspect in the next section.

4 Dispersion of nanoparticles in polymer matrices

A major challenge in achieving the desired properties of polymer nanoparticle blends is in controlling the state of dispersion of the particles. As a result, extensive research[2,16,56,120,121] is devoted over the last two decades to understand and develop the strategies for controlling the dispersion of PGNPs. In this section, we briefly describe the thermodynamical arguments allowing us to understand the dispersion of nanoparticles in polymer matrices.

4.1 Dispersion of bare nanoparticles

We begin our discussion with the dispersion of spherical bare nanoparticles, *i.e.* without any grafting agents, in polymer matrices. For simplicity, we assume that the enthalpic interactions between the particle and the polymer are neutral (achieved by considering similar chemical nature for both the nanoparticles and polymers). In this case, the dispersion of particles simply depends on the balance of entropic forces acting in the system. There will be two components of entropy: (a) the mixing entropy and (b) the stretching entropy associated with the matrix chains. Given the neutral interactions between

the particles and polymers, dispersion increases the entropy and decreases the free energy of the system. This free energy F_{mix} directly scales with the volume fraction of the particle ϕ_p and inversely scales with the volume ($\sim R_{np}^3$).[2,42]

$$F_{mix} \sim \left(\frac{\phi_p}{R_{np}^3}\right) \ln \phi_p \quad (31)$$

On the other hand, the host chains have to stretch in order to accommodate the particles. This, in turn, evokes an entropic penalty as stretching would limit the number of accessible conformations of the matrix polymers. The free energy $F_{stretch}$ associated with stretching increases with increase in the particle size, with respect to the radius of gyration R_g of the polymer.[2,42]

$$F_{stretch} \sim \left(\frac{R_{np}}{R_g}\right)^2 \quad (32)$$

The balance of F_{mix} and $F_{stretch}$ controls the dispersion of bare particles in polymer matrices. For all $R_{np} < R_g$, the entropic gain F_{mix} due to mixing will be larger than the stretching penalty $F_{stretch}$ of the chains. Thus, we expect the particles to disperse for $R_{np} < R_g$, and not dispersed otherwise. Using polyethylene (PE) nanoparticles in polystyrene (PS) matrices, Mackay *et al.*[22] demonstrated the possibility of dispersing particles by harnessing the relative size ratio of particles and polymer chains (see Fig. 2a). Despite the enthalpic unfavourability of PE in PS, small nanoparticles of PE displayed good miscibility in PS matrices due to the gain in translational entropy. Building on this understanding, we will now move towards the dispersion of PGNPs and how entropy allows harnessing dispersion of particles in polymer matrices.

4.2 Dispersion of polymer grafted nanoparticles

The grafted polymers in PGNPs provide additional avenues to control the dispersion of PGNPs in polymer matrices. As discussed in Section 3, the conformations of grafted chains depend on various factors including grafting density σ and the molecular weight of the grafted polymer M_g. In Fig. 2(b), we display transmission electron micrographs of PS grafted silica nanoparticles mixed with linear PS of molecular weight M_m = 142 kDa (data adopted from ref. 33). Since the grafted and matrix polymers are of same chemical nature, the enthalpic interactions are neutral, *i.e.* the Flory Huggins parameter $\chi = 0$. Thus, the dispersion will be dictated by the entropic interactions (to be discussed below) at the particle–polymer interface. A control over σ and M_g yields a rich control over the dispersion morphology of PGNPs varying from spherical clusters to strings, sheets, and complete dispersion. In a recent review, as shown in Fig. 2(c), Kumar *et al.* summarized the control over dispersion of PGNPs by controlling the σ, M_g and its ratio with the molecular weight M_m matrix polymer, $f = M_g/M_m$. In what follows, we provide thermodynamic arguments for understanding the dispersion of PGNPs in polymer matrices.

Here, we will begin with the well-developed theories on the mixture between polymers and flat brushes to discuss the associated free energies.[122,123] We consider no enthalpic interactions between the grafted and matrix polymers, *i.e.* we limit our discussion to systems with $\chi = 0$. Upon mixing linear polymers with grafted brushes, the free energy will have contribution from the elastic energy required to stretch the grafted chains F_g and from the excluded volume interaction induced entropic repulsion from the matrix polymers F_m. At low grafting densities, the effective free energy could be approximated to ref. 122

$$F \sim \frac{h_g^2}{N_g a^2} + \frac{a^3}{N_m}\frac{N_g^2}{h_g^3} \quad (33)$$

where N_m is the degree of polymerization corresponding to matrix polymers. An interplay between stretching (mediated *via* N_g) and entropic repulsion (mediated *via* the ratio of N_m and N_g) will decide the extent of dispersion. For $N_m \approx \sqrt{N_g}$, the entropic repulsion due to excluded volume is of the order of kT and can be neglected. Thus, minimizing $F = F_g$ yields $h_g \sim aN_g^{1/2}$, which matches with the radius of gyration of the polymer in melt conditions. With an

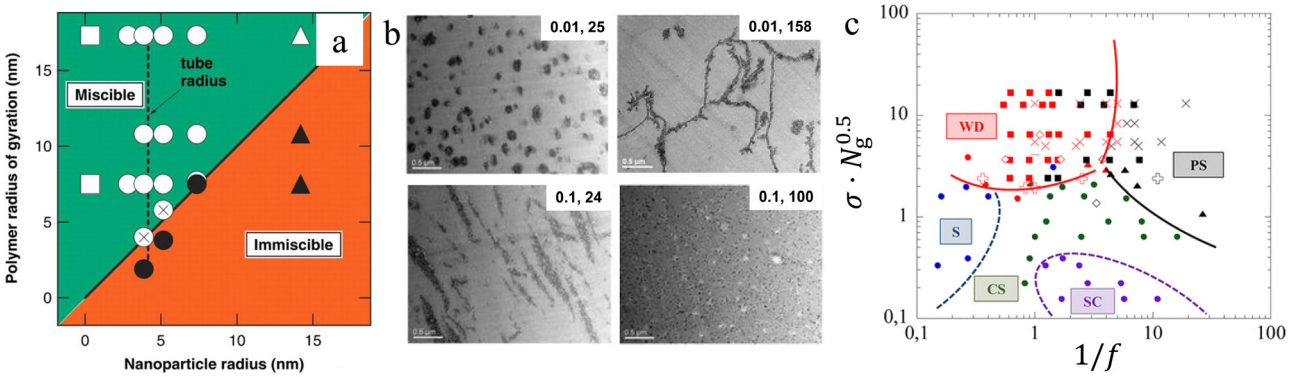

Fig. 2 Dispersion of nanoparticles in polymer matrices: (a) phase diagram, polymer radius of gyration *vs.* nanoparticle radius, differentiating the miscible (dispersed nanoparticles) and immiscible states of polymer + nanoparticle mixtures. (b) TEM images capturing the dispersion of particles with different grafting densities σ and grafting molecular weight M_g. Each micrograph is defined by values corresponding to σ (in the units of chains per nm^2), M_g (in the units of kg mol^{-1}) at the top right corner. The matrix molecular weight is kept constant at M_m = 120 kg mol^{-1}. (c) Phase diagram capturing the dispersion states of PGNPs in bulk. Here, f is the ratio of the graft to the matrix length. Panel (a) is adapted from ref. 22 and panels (b) and (c) are adapted from ref. 33.

increase in grafting density, the grafted chains begin to swell and beyond $\sigma^*/a^2 \equiv 1/{h_g}^2$, the swollen chains overlap. This leads to a grafting density dependent entropic repulsion F_m. Thus, the effective free energy takes the form[122]

$$F \sim \frac{{h_g}^2}{N_g a^2} + \frac{a^3}{N_m}\frac{{N_g}^2\sigma^*}{h_g a^2} \quad (34)$$

where the effective excluded volume term is $h_g a^2/\sigma^*$ instead of ${h_g}^3$. Minimizing eqn (34) yields $h_g \sim a(\sigma^*/N_m)^{1/3}N_g$. Thus, at large σ, the thickness of the grafted layer is an explicit function of σ and N_m. The brush in this regime is denoted as the wet-brush. With further increase in σ, the volume fraction of the grafted chains in the brush is of the order of unity. For a stretched wet-brush, this corresponds to $\sigma^* \approx {N_m}^{2/5}/{N_g}^{6/5}$. In such cases, a partial interpenetration between the grafted and the matrix polymers is conceivable over a small thickness ξ. As a result, the free energy scales with ξ as[122]

$$F \sim \frac{\sigma^*}{a^2}\frac{\xi^2}{N_g a^2} - \xi\frac{a^3}{N_m}\left(\frac{1}{a^3}\right)^2 \quad (35)$$

The first term on the right corresponds to the additional elastic energy for stretching the chains by ξ and the second term corresponds to the entropic gain allowing for the diffusion of matrix polymers into the graft layer. The grafted and matrix polymers tend to disperse if the elastic stretching energy is larger than the entropic gain. The brush in this regime is denoted as the dry-brush. Upon minimizing eqn (35), we obtain $\xi = (aN_g)/(2\sigma^*N_m)$. Using the packing constraints, we could show $h_g \approx aN_g\sigma^*$. When the penetration length ξ is of the order of h_g, the dry-brush becomes the wet-brush. For large matrix chains, $N_m > N_g$, it could be visualized that the energy cost for diffusing into the grafted layer would be significantly higher. Thus, we may expect a dewetting zone at the particle–polymer interface. Such large grafting densities have been utilized in the literature to achieve autophobic dewetting.[55,124,125] We summarize the dimensions (h_g, ξ) corresponding to the different conformations in Table 1.

Now, let us focus on grafted chains on curved surfaces, as will be the case of polymer grafted to nanoparticles. As discussed in Section 4, the number density of grafted chains decreases as we progress from the center to the edge of a polymer grafted nanoparticle in the CPB regime.[48] Thus, the grafting density σ and the interpenetration width ξ discussed in eqn (35) and (34) should be rescaled with the radius R_{core} of the core of PGNPs. Trombly and Ganesan[126] showed that the effective grafting density and the thickness of the graft layer of the curved surface takes the form

$$\sigma_{curved} = \frac{\sigma {R_{core}}^2}{\left(R_{core} + h_g\right)^2} \quad (36)$$

$$\frac{h_{curved}}{h_g} = \left(\frac{R_{core}}{R_{core} + h_g}\right)^y \quad (37)$$

where $y = 2$ for dry brushes and $y = 2/3$ for wet brushes. In addition, they revealed that the interpenetration width ξ_{curved} can be related to the ξ of the flat brushes as ref. 126

$$\frac{\xi_{curved}}{\xi} = \left(1 + \frac{h_g}{R_{core}}\right)^{2/3} \quad (38)$$

Table 1 Different conformations and their corresponding values of h_g and ξ for a flat brush

	Flat brush	
Conformation	h_g	ξ
Mushroom (ideal)	$aN_g^{1/2}$	h_g
Mushroom (swollen)	$aN_g^{3/5}$	h_g
Wet-brush	$aN_g\left(\frac{\sigma^*}{N_m}\right)^{1/3}$	h_g
Dry-brush	$aN_g\sigma^*$	$\frac{a}{2\sigma^*}\left(\frac{N_g}{N_m}\right)$

For large particles $R_{core} \gg h_g$, since the curvature effects would be minimal, the flat brush behaviour would be restored.

To summarize, entropic constraints due to the brush/host chain interactions are significant and can favour the mixing of the nanoparticles with the host chains or contribute toward phase separation between particles and host chains. The host/brush interactions are determined by the parameters N_g, N_m and σ. When the grafted chains are sufficiently long ($N_g \gg N_m$) and σ is sufficiently low, that is, $\sigma^*{\cdot}{N_g}^{1/2} < (N_g/N_m)^{1/2}$, then the host chains can interpenetrate or wet the brush layer, thereby forming a so-called wet brush.[2,33,127] This would promote miscibility between the particles and the host chains. On the other hand, when the grafting density is very high and $N_g \ll N_m$, specifically, when $\sigma^*{\cdot}{N_g}^{1/2} < (N_g/N_m)^{1/2}$, the host chains are partially excluded from the grafted layer, thus forming a dewetting interface between the polymer and the particle.

4.3 Physical confinement allows harnessing dispersion

In various applications, PNCs are used in the form of films, often with thicknesses that are of the order of the unperturbed size of the matrix polymer. In such confined geometries, several studies reveal that the polymers are strongly deformed resulting in restrictions in their conformational degrees of freedom. Will such confinement-induced molecular deformations and therefore the resulting reduction in the conformational entropy of the chain affect the dispersion of nanoparticles?

To address this aspect, we[54] reported experiments on PS grafted gold nanoparticles dispersed in PS thin films with different thicknesses. For a systematic control over the entropy at the particle–polymer interface, M_g and M_m are varied in a way that $f = M_g/M_m$ varies from 0.033 to 2.5. As described in Section 4.2, PGNPs in composites with $f \ll 1$ is expected to phase segregate and the PGNPs in systems with $f > 1$ will stay dispersed. Scanning electron micrographs capturing the dispersion behaviour of PGNPs in composites with $f = 0.033 \ll 1$ are summarized in Fig. 3(a) and (b). Expectedly, PGNPs mixed with polymer films of thickness h = 65 nm exhibit cluster formation at the air surface with no evidence of dispersion (see Fig. 3(a)). On the other hand, for thinner films shown in

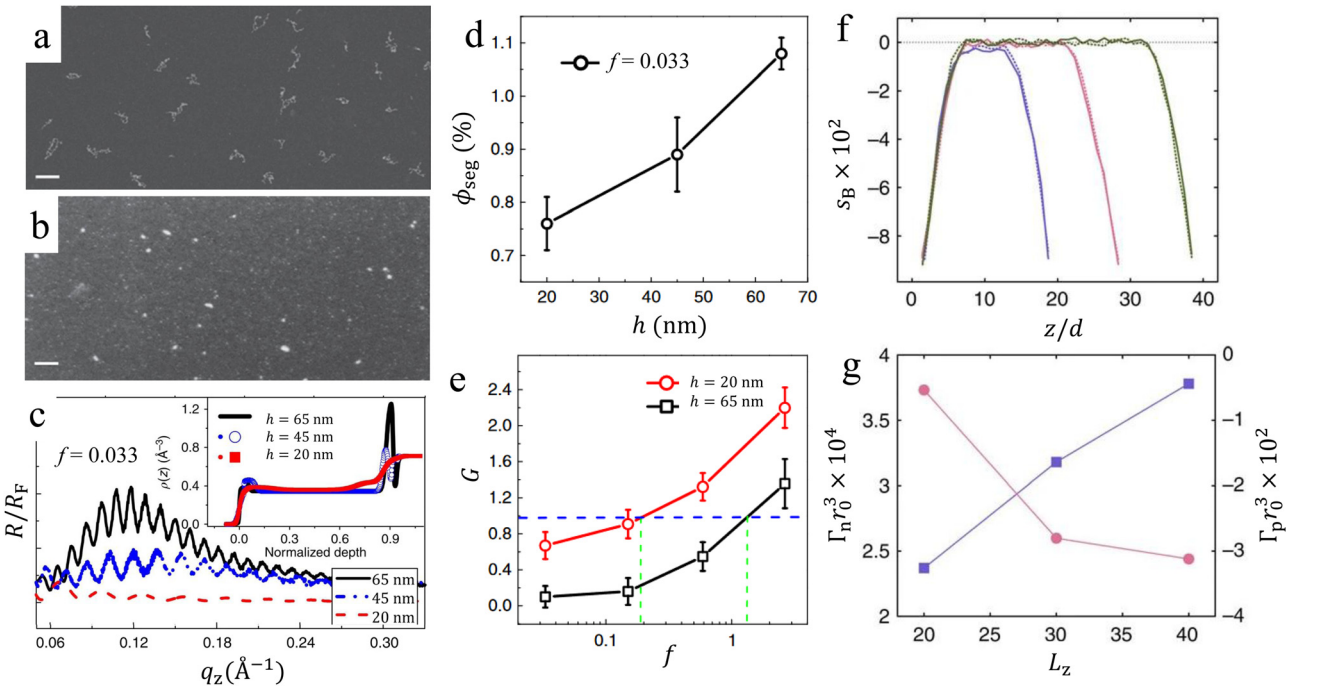

Fig. 3 Confinement enhances the dispersion of PGNPs in polymer films: scanning electron micrographs of composite films with f = 0.033 for (a) h = 65 nm and (b) h = 20 nm. Scale bars in (a) and (b) correspond to 200 nm and 100 nm, respectively. (c) Fresnel normalized reflectivity R/R_F is shown as a function of normal wave vector q_z for composite films of three different thicknesses as defined in the panel. The electron density profiles obtained from the modelling of reflectivity curves are provided in the inset of (c). (d) Fraction ϕ_{seg} of segregated particles as a function of film thickness. (e) Dispersity $G = \phi_{bulk}/\phi_{seg}$ is shown as a function of f for films of two different thicknesses. (f) Bond orientational order parameter s_B along the film thickness z/d is shown for simulation boxes of three different thicknesses. (g) The excess surface absorption (normalized with appropriate volumes) of nanoparticles (Γ_n) and polymers (Γ_p) is shown as a function of the thickness L_z of the simulation boxes. All data are adapted from ref. 54.

Fig. 3(b), we witness apparently well-dispersed PGNPs (small bright dots) in the background of small clusters (brighter and relatively larger dots) at the surface. This suggests an improved dispersion of PGNPs in thinner films.

X-ray reflectivity measurements on composite films of different thickness provide further support to this observation.[54] Apart from probing the film thickness (*via* Kiessig fringes), XR also allows probing the differences in the electron density contrasts along the film thickness (refer to Section 2.2). Thus, any preferential segregation of particles to the air surface or to the substrate interface, creating electron density modulation, could be captured from the raw data (without detailed modelling). In Fig. 3(c), Fresnel normalized XR profiles are shown for composite films of three different thicknesses, h = 20, 45, and 65 nm. The Fresnel part gives the wave-vector dependence of reflectivity *i.e.* $R_F \sim q_z^{-4}$ (see eqn (3)). For an ideal film with homogeneous density along the film thickness, the Fresnel normalized reflectivity should be oscillating, reflecting the thickness of the film, but flat without any additional q_z-dependence. Clearly, as shown in Fig. 3(c), thicker films reveal a strong additional modulation, whose amplitude indicates the strength of the gradient in electron density, and the peak position indicates the thickness of such electron density modulation. This modulation reflects the segregation of PGNPs at the substrate interface. Interestingly, the amplitude of this additional modulation also decreases with the decrease in the film thickness. This suggests a decrease in the extent of interface segregation with h.

To extract quantitative information on dispersion and the preferential segregation to the surfaces, we[54] performed detailed modelling of XR data (refer to eqn (5) and (6)) using an effective three-layer description of the film: a layer at the air surface, followed by bulk, and then a layer at the substrate interface. The thickness dependence of electron density extracted from such modelling is shown in the inset of Fig. 3(c). Supporting the Fresnel normalized reflectivity, the thickness dependence of electron density profiles reveals a strong segregation of particles at the substrate interface. There is an apparent decrease in the density of particles at the substrate interface with a decrease in film thickness. This aspect is quantified by discretizing the electron density into three effective layers and the fraction of PGNPs residing at the respective layers are defined as ϕ_{sur}, ϕ_{blk}, and ϕ_{int} with a restriction such that the total fraction $\phi_p = \phi_{sur} + \phi_{blk} + \phi_{int}$. For a given bulk fraction of ϕ_p = 1.2 wt%, a systematic decrease in the segregated fraction $\phi_{seg} = \phi_{sur} + \phi_{int}$ of PGNPs can be witnessed with decrease in film thickness (see Fig. 3(d)). This is interesting, as the entropy at the particle–polymer interface enables complete phase separation. To visualize this more clearly, Fig. 3(e) shows the extent of dispersion by plotting $G = \phi_{blk}/\phi_{seg}$ as a function of f. As expected, G increases with increase in f. For all f, G values corresponding to thinner films

are larger than those of the thicker films. Clearly, thickness serves as an additional parameter contributing to the dispersion of PGNPs in polymer films.

CGMD simulations using bead spring chains with FENE reveal further microscopic insights into the enhanced dispersion of PGNPs with the decrease in film thickness. To reflect the thickness-induced confinement, periodic boundary conditions were used in x and y, while z is confined between two parallel surfaces. The distance L_z between the parallel surfaces will act as a proxy to the film thickness h. Simulation parameters were carefully chosen to match the experimental parameters like σ, f and the size ratio of nanoparticles with the grafted and matrix polymers. Please refer to Chandran *et al.*[54] for further details. Simulations corroborate the enhanced dispersion of PGNPs with confinement.[54] To quantify the potential changes in the chain structure of the matrix polymers, we deduced the bond orientational order parameter $s_B = 0.5[3\langle\cos^2\theta_{j,z}\rangle_i - 1]$, where $\theta_{j,z}$ is the angle between the bond (formed between j and $j-1$ monomers) and z-axis (axis along the film thickness). As shown in Fig. 3(f), s_B of chains in the bulk is negative for thinner films, while for thicker films, $s_B = 0$. This suggests that the chains residing in thinner films are ordered, indicating a reduced conformational entropy. Such reduced conformational entropy is manifested in the excess surface adsorption of particles (and polymers), defined as $\Gamma_i = \int_0^{L_z/2}[\rho_i(z) - \rho_{i,\mathrm{bulk}}]\mathrm{d}z$, where i corresponds to polymers or nanoparticles. As shown in Fig. 3(g), the surface excess of nanoparticles Γ_n decreased with decrease in L_z, while Γ_p increased with decrease in L_z. This suggests that the thinner films minimize density gradients, likely due to energetic penalty as the interfaces in thinner films are not decoupled as in thicker films. Similar observations were also reported for polymer blend films.[128] Our results clearly demonstrate that physical confinement allows controlling the dispersion of particles that are otherwise expected to be phase-separated. Thus, confinement provides a new lever to control the dispersion and hence a whole spectrum of physical properties that depend on the state of dispersion of particles.

Having understood the processes controlling the dispersion of particles in polymer matrices, in the next sections, we reveal the manifestations of the dispersed states in controlling the physical characteristics of PNC films. The interfacial entropic interactions between grafted and matrix polymers impose constraints on molecular mobility, leading to notable variations in viscosity and glass transition behaviour. These effects are particularly pronounced in thin films, where confinement amplifies interfacial entropy-driven phenomena, as discussed in the following sections.

4.4 Particle–polymer interface controls glassy behavior

Glass transition temperature and glassy dynamics are important parameters allowing the control of the processing of various polymeric structures. Accordingly, intensive efforts were devoted to understanding the glass transition behaviour of PNCs.[129–131] Driven by the enormous data on the thickness dependence of glass transition temperature (T_g) of thin polymer films, initial efforts were devoted to understanding the T_g of PNC films in the same framework.[125] Here, the interparticle distance h_p acts as a proxy for the thickness of polymer films. Conceivably, control over the fraction ϕ_p of particles allows controlling h_p. Assuming a random dispersion of particles allows a simple relation between h_p and ϕ_p as $h_p \sim 2R_{pgnp}\sqrt[3]{\phi^{rcp}/\phi_p} - 1$, where $\phi^{rcp} = 0.638$ is the random close packing fraction.[54,125] Bansal *et al.*[125] performed pioneering experiments with different fractions of bare silica nanoparticles dispersed in polystyrene matrices. Fig. 4(a) displays the equivalence between pristine PS thin films and PS composites in bulk (adapted from Bansal *et al.*[125]). Qualitatively, the h_p dependence of T_g for composites followed a dependence similar to that of the dependence of thickness dependent the T_g of pristine polystyrene films coated on neutral surfaces (refer to Bansal *et al.*[125] for other equivalent definitions h_p^*, h_p^{**}, and h_p^{***} of the interparticle spacing). Here, we note that for wetting surfaces, polymer films and polymer nanocomposites exhibit an increase in T_g with decreasing h_p.[132] Given this background, it is natural to ask if the dependence of T_g will be the same for PGNPs with different f or σ. To shine light on this aspect, we discuss our experiments[54,55,58] on PS grafted gold nanoparticles dispersed in PS films. For this purpose, in Fig. 4(b), we summarize the T_g as a function of ϕ_p for composite systems with different f values. For $f = 0.033 \ll 1$, we observe a systematic decrease in T_g with ϕ_p. This is in accordance with the summary plot shown in Fig. 4(a). However, for the same ϕ_p, the extent of decrease in T_g is smaller for $f = 0.15$ in comparison with $f = 0.033$. More interestingly, composites with $f > 1$ display enhancement in T_g with ϕ_p. Using coarse-grained molecular dynamic simulations, we revealed[95] that systems with $f \ll 1$ have decreased monomer density at the particle–polymer interface. The presence of such dewetting regions around the polymer–particle interface creates additional free volume, which might explain the decrease in T_g for composites with $f < 1$. On the other hand, for composites with $f > 1$, the grafted chains and the matrix chains interpenetrate nicely, thereby imposing additional restrictions on the mobility of the monomers. This might underlie the observed enhancement in T_g. Recent theory and simulations on freestanding polymer films highlight that the deviations in the chain dynamics at substrate interfaces may underlie modifications in caging constraints at the surface and its manifestations to the local elastic barrier for the relaxation.[133] We anticipate that similar mechanisms might underlie the enhanced (or suppressed) dynamics at the particle–polymer interface of $f < 1$ (or $f > 1$) systems.[43,54,55,87,132,134] In addition, as discussed in the last section, we revealed that mere physical confinement increases the extent of dispersion of particles that are otherwise phase segregated. Such increased dispersion, in turn, manifests into a larger number of dewetting interfaces within the polymer film. Thus, as shown in Fig. 4(c), thinner films exhibit larger deviations in T_g for any given ϕ_p. To summarize, these results demonstrate that harnessing entropy at the polymer–particle interface, quantified *via f*,

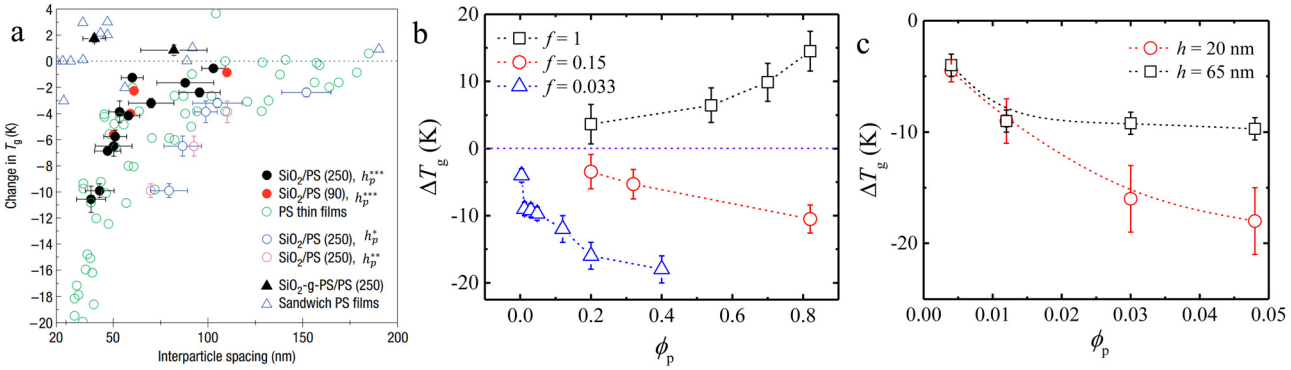

Fig. 4 Dispersion state allows controlling glass transition temperature: (a) deviations in glass transition temperature T_g is shown as a function of interparticle spacing. Also shown are the deviations in T_g for pristine polystyrene films of different thicknesses. (b) Deviations in T_g *i.e.* ΔT_g is shown as a function of the fraction ϕ_p of particles mixed with polymer films of thickness 65 nm. Data corresponding to composites with three different f values, as defined in the panel, are shown. Horizontal dashed lines in (a) and (b) correspond to the bulk T_g of polystyrene. (c) ΔT_g *vs.* ϕ_p for films of two different thicknesses as defined in the panel. Data shown in (a) are reproduced from ref. 125. Data shown in (b) and (c) are replotted from ref. 54, 55 and 58.

allows a systematic control over the glass transition behavior of PGNP-based polymer composites.

4.5 Controlling interfacial entropy yields giant changes in viscosity

Viscosity is a crucial parameter, in addition to designing processing conditions, allowing the interpretation of the molecular characteristics of polymers, free volume content, and the dispersion states of nanoparticles in polymer matrices. PGNPs provide novel pathways to control the viscosity of polymers *via* the interfacial layer (IL) between the matrix and the grafted polymer.[45,58,60,61,70,87,135,136] As discussed in Section 4.2, the width ξ of the interfacial layer can be experimentally controlled by tuning the size of the particle, f, and σ. Thus, extensive work has been devoted to developing an understanding of how the viscosity of PNCs depends on these experimental parameters controlling the dispersion states and the nature of IL in PNCs.[58,61,70,87,135] Due to interfacial effects of PGNPs, research has indicated both an increase and a decrease in viscosity upon the introduction of particles. The increase in viscosity is well-documented and can be characterized by the Batchelor and Einstein relation.[137] Conversely, certain investigations have reported a reduction in viscosity associated with particle incorporation.[138–141] A variety of models have been proposed to elucidate this phenomenon.[139,142] Here, we will provide a brief of these models.

4.5.1 Models in viscosity analysis. Two significant models that describe viscosity in such systems are the Batchelor and Einstein relation[137] for particle suspensions and the Wang–Hill model[140] for polymer in solution. While both models address the influence of dispersed entities on fluid viscosity, they apply to fundamentally different systems and account for distinct physical interactions.

The Einstein-Batchelor relation provides a relation between the effective viscosity and the concentration of the inclusions in a dilute suspension of spherical particles.[137] This relation, which builds on earlier work conducted by Albert Einstein,[143] is particularly useful in colloid science and rheology for understanding how suspended particles increase a fluid's viscosity.[144,145]

$$\eta_{\text{eff}} = \eta_0(1 + 2.5\phi), \tag{39}$$

which describes the viscosity of a fluid with suspended spheres at low concentrations. Batchelor[137] extended this theory by adding a second-order correction for interparticle interactions, yielding:

$$\eta_{\text{eff}} = \eta_0(1 + 2.5\phi + 6.2\phi^2), \tag{40}$$

where η_0 is the solvent viscosity and ϕ is the particle volume fraction. In suspensions, viscosity increases with increasing particle concentration due to enhanced hydrodynamic interactions and crowding effects.

In contrast, several reports reveal that the PNCs may exhibit a decrease in the viscosity, in comparison with the pristine polymers. Addressing this aspect, here we highlight the Wang–Hill (WH) model[140] describing the intrinsic viscosity $[\eta]$ of polymer solutions, incorporating polymer–solvent interactions, molecular weight, and chain conformation. This model describes a negative intrinsic viscosity in the framework of the presence of an interfacial layer at the NP–matrix interface with a viscosity and density different from that of the bulk. The WH model for intrinsic viscosity $[\eta]$ is often expressed as:

$$[\eta] = \lim_{\phi_p \to 0} \frac{\eta_{\text{PNC}} - \eta_p}{\phi_p \eta_p} \tag{41}$$

Both models are essential in rheology for predicting fluid viscosity. The Wang–Hill model applies to polymeric solutions, while the Batchelor equation describes particle laden fluids. Understanding them aids in optimizing industrial processes involving polymers and suspensions. These are the classical models used to describe viscosity changes in polymers. However, when PGNPs are introduced into the polymer matrix, forming PNCs, numerous additional parameters come into play, influencing the flow behaviour. In PNCs, the presence of PGNPs and the interfacial layer significantly impacts the system's rheology, which can be better understood through

modelling approaches that incorporate entropic contributions. In the following section, we explore how these interfacial effects influence the overall transport properties, providing deeper insights into the role of entropic parameters in governing the behaviour of PNCs.

Various studies have been conducted to understand the rheological behaviour of polymer nanocomposites (PNCs) through both experimental and computational approaches. In particular, the work of Kalathi *et al.*,[135] including experiments and simulations, highlighted how the viscosity of PNCs changes in miscible (athermal) and immiscible (thermal) blends of polymers with PGNPs. As shown in Fig. 5, Kalathi *et al.* summarized the role of the diameter of the nanoparticles in controlling the viscosity η of PNCs in comparison with the viscosity η_p of the neat polymers. They investigated how nanoparticle (NP) incorporation affects polymer melt viscosity, focusing on polymer–NP interactions, NP size, and polymer chain length. A "viscosity crossover" criterion is introduced to predict the impact of NPs on viscosity based on the properties of both the polymer and the nanoparticles. Fig. 5(a) highlights systems with chemically similar polymers and NPs, showing a transitional point where the viscosity of nanocomposites either exceeds or falls below that of the pure polymer melt, influenced by the NP size and polymer chain characteristics. Fig. 5(b) addresses chemically dissimilar systems, where immiscibility often leads to increased viscosity due to poor dispersion and NP aggregation. In cases of moderate attraction between polymers and NPs, viscosity trends resemble those in miscible systems. These insights are crucial for designing nanocomposites with tailored flow properties.

Most studies on PNCs have focused on their bulk properties;[148] however, numerous applications utilize them as coatings and thin films.[26,125] In such confined systems, the strong confinement effects and the presence of a substrate interface can introduce new aspects that influence viscosity.[149–155] Therefore, it is crucial to measure the viscosity of thin films and understand interfacial dynamics to enhance processability and optimize their applications. In bulk systems, oscillating rheometry is the standard technique for viscosity measurements, but for nanoscopic thin films, viscosity measurements are more challenging. X-ray scattering techniques have been employed to determine thin film viscosity; however, these methods face limitations, particularly when dealing with highly loaded particle systems. To address these challenges, Swain *et al.*[87] utilized the AFM-based force–distance technique (discussed in Section 2.3) to extract viscosity and analyze interfacial effects, including segmental changes.

The force–distance curves obtained for PNC films at various temperatures are illustrated in Fig. 6(a) and (b) for both PNC types, with a fixed PGNP volume fraction. Clearly, the reduction in viscosity with increasing temperature affects the force–distance curves, as evidenced by the decrease in both the pull-off force and the curvature of the liquid bridge. The adhesion force and force–distance profile during tip retraction vary with temperature for both f contents, highlighting the influence of f on the shape of the force–distance curves, as seen in Fig. 6(c).

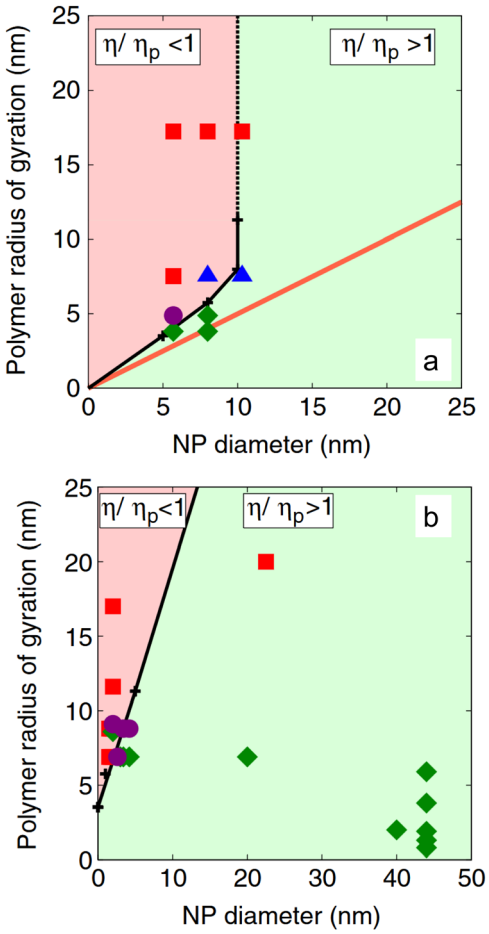

Fig. 5 Polymer radius of gyration *vs.* nanoparticle (NP) diameter and viscosity ratio of nanoparticle blends: (a) experimental data for athermal systems, adapted from ref. 139 and 146. Systems above the solid orange line are predicted to be miscible. The black "viscosity" line represents extrapolated results from simulations. (b) Corresponding data for "thermal" NP–polymer systems. Experimental data points are represented as follows: (□) for $\eta/\eta_p < 1$, (◊) for $\eta/\eta_p > 1$, (○) for $\eta/\eta_p \approx 1$ at low NP loading, and (Δ) for cases where viscosity (η) initially increases with NP loading and subsequently decreases. Only the viscosity line is displayed, with data from ref. 5, 142 and 147, adapted from ref. 135.

To investigate this phenomenon, we modelled the force–distance curves using eqn (17)–(20) and extracted the viscosity of the films. Viscosities for all samples are presented in Fig. 6(d) and (e) as a function of temperature for all volume fractions. As expected, a decrease in viscosity with temperature is observed. PNCs with $f = 1$ exhibit a significantly higher viscosity than bulk polystyrene (PS), with this difference becoming more pronounced as the volume fraction of PGNPs increases. Conversely, PNCs with $f = 0.15$ show a viscosity reduction compared to PS. Fig. 6(f) illustrates normalized viscosity as a function of volume fraction at different temperatures. The data reveal distinct pathways of viscosity change, with an increasing ratio for PNCs with $f = 1$ and a decreasing ratio for those with $f = 0.15$. The giant increase in the viscosity increase for systems with $f = 1$ surpasses predictions by the Batchelor–Einstein model.[156,157]

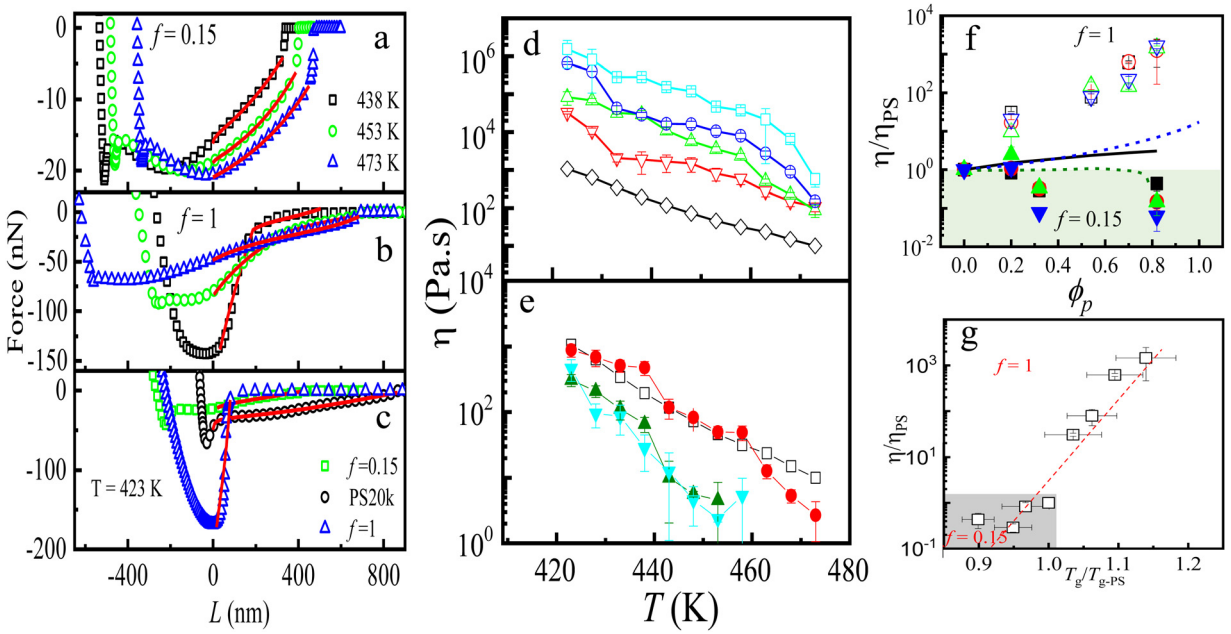

Fig. 6 Harnessing entropy for controlling the viscosity of PNCs: force–distance curves shift with temperature, showing distinct behavior for samples with (a) f = 0.15 and (b) f = 1; (c) pure PS and high-f PNC samples reveal the impact of filler content on F–D curves at 423 K. Temperature dependent viscosity of (d) f = 1 and (e) f = 0.15 samples at different volume fractions of particles. The open black squares represent the η of bulk PS of molecular weight 19 kDa. In (d), red, green, blue and cyan symbols correspond to ϕ_p = 0.21, 0.59, 0.77, and 0.90, respectively. In (e), red, green and cyan symbols correspond to ϕ_p = 0.20, 0.34, and 0.83, respectively. (f) Normalized η for all the PNC samples with respect to the bare PS films, η_{PS}, as a function of ϕ_p is shown for both f = 1 (open symbols) and f = 0.15 (closed symbols). Also shown are the predictions of Bactchelor-Einstein equation (continuous black line), WH predictions with χ = 4 (dashed blue lines) and χ = 0.0001 (green dashed lines). (g) η/η_{PS} as a function of $T_g/T_{g\text{-}PS}$. The figure is adapted from Swain *et al.*[87]

Our study highlights substantial viscosity enhancements for PNCs with f = 1, supported by enthalpically matched and unentangled chain structures that mitigate the effects of filler attraction and entanglement interactions. Furthermore, our findings align with recent reports on f, attributing anomalous viscosity reduction to an interfacial viscosity lower than the bulk viscosity for lower filler contents.[87] The results emphasize the significant impact of f on viscosity due to interfacial entropic interactions between the polymer matrix and grafted chains. The effects are amplified at high ϕ_p.

As previously discussed, different models, including the Batchelor–Einstein (BE) and Wang–Hill (WH) models, describe viscosity changes in the polymer. The WH model, in particular, predicts a negative intrinsic viscosity due to the presence of an interfacial layer at the nanoparticle (NP)–matrix interface, which exhibits distinct viscosity and density compared to the bulk material. In Fig. 6(f), the blue and dark green dashed lines correspond to the WH model for different interfacial parameter χ_{12} values, showing both increase and decrease in viscosity. Although varying χ aligns with our findings, the observed viscosity variations are significantly greater. Previous studies[141,146,158] have linked viscosity increases to dynamics at reptation length scales, while decreases relate to shorter length scales or segmental-level dynamics influenced by the interface. Our observations indicate both increases and decreases for systems with identical particle–polymer interfaces, prompting us to propose a single mechanism for these viscosity (η) changes. We found that interfacial chain penetration ξ increases with volume fraction (ϕ), indicating a stronger interaction between grafted and matrix monomers at higher f. This emphasizes the need to explore additional experimental parameters sensitive to segmental-level changes. Recognizing that glass transition processes occur at the segmental level, we measured glass transition temperature (T_g).

We correlated changes in T_g with η to illustrate overall behavior, plotting η/η_{PS} against normalized T_g ($=T_g/T_{g\text{-}PS}$) in Fig. 6(g). The entire sample set aligns along one master curve, suggesting that segmental dynamics predominantly influence viscosity changes. Lower normalized T_g values indicate reduction in both T_g and η, while higher values correspond to increases in both metrics. Thus, interfacial entropic interactions between PGNPs and matrix polymer chains alter interfacial segmental dynamics, leading to the observed viscosity changes in PNCs.

4.6 Hydrodynamic interactions between the particles in the polymer matrix

Dynamics at the nanoparticle–matrix interfaces often deviate from the bulk. As discussed in the previous sections, our group and others have established the relationship between the control over the interfacial layer (as *e.g. via* f, σ, and particle size) and deviations in physical properties including glass transition temperature and viscosity.[1,136,159,160] Here, we highlight our work quantifying the nature of dynamics and the

boundary conditions (quantified *via* interfacial slip) at the PGNP–polymer interface.[43,136] Addressing this aspect, we probed temperature-dependent and confinement-dependent microscopic dynamics by employing CGMD simulations[43] and XPCS measurements[136] on PNC films made of PGNPs with controlled f and σ.

CGMD simulations allowed us to probe the role of interfacial entropy, tuned *via* f and σ, in the boundary conditions between PGNPs and polymer interfaces.[43] The results are summarized in Fig. 7(a) and (b) by plotting the interfacial slip length δ as a function of f and σ. The dewetting interfaces, with small f, result in a large slip, while the wetting interfaces (large f) display a smaller interfacial slip. Clearly, the width of the interfacial layer *i.e.* extent of matrix chain penetration into the grafted chains controls the slip length. At smaller f, the smaller penetration leads to a larger slip and a larger f results in a larger penetration and consequently smaller slip length as shown in Fig. 7(a). On the other hand, keeping f fixed while increasing the grafting density σ, the δ decreases (Fig. 7(b)), which contradicts the conventional understanding, *i.e.* a higher grafting density is predicted to exhibit dry brush (due to a lower degree of mixing between graft and matrix chains) and hence a larger slip effect. However, the present behaviour reveals the opposite, meaning larger σ results in smaller δ. This behaviour is due to the effect of the nanoparticle curvature.[43] Due to the large curvature (small core radius), we may expect that the grafted chains will experience a progressive decrease in crowding with an increase in the radial distance from the core. Consequently, grafted chains could interpenetrate with the matrix chains for PGNPs with higher σ. Such increased interpenetration might underlie the decrease in δ with increase in σ.

XPCS measurements allowed us to probe the correlations between such interfacial slip and macroscopic viscosity.[136] Especially, the temperature dependence of the relaxation time τ, reflecting the microscopic dynamics of PGNPs in polymer thin films of different thicknesses, is probed and compared with the expected temperature dependence of viscosity. Fig. 7(c) summarizes the results of systems with f (=0.033) $\ll$ 1. Interestingly, compared to the viscosity ratio η_i/η_{473}, the renormalized relaxation time differs significantly while these parameters are expected to be proportional in the absence of the reduced effective interface viscosity. The deviation is clearly visible using the anomaly parameter ζ, defined as the ratio of the normalized τ to normalized η, as shown in Fig. 7(d) (defined in the caption). Clearly, the deviation increases under confinement as well as with decreasing temperature approaching the glass transition of the matrix. These results suggest that the viscosity at the particle polymer interface, *i.e.* the interfacial

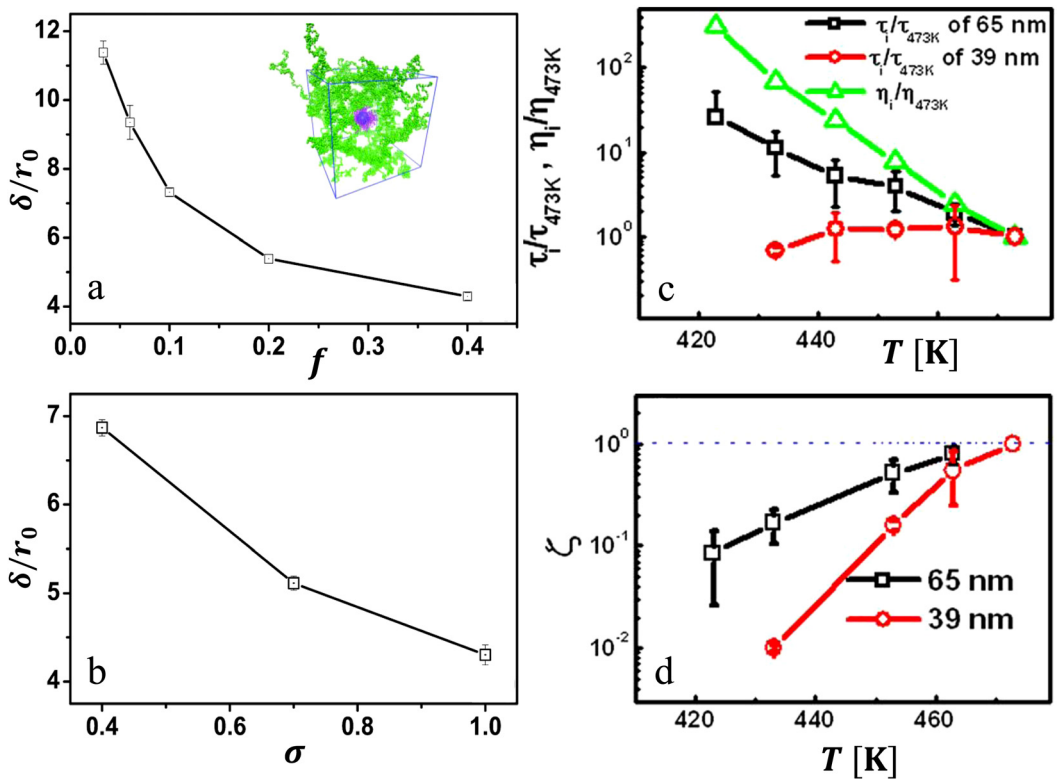

Fig. 7 Hydrodynamic interactions at particle–polymer interface: (a) slip length experienced by the particle at the particle–matrix interface as a function of entropic compatibility parameter f; (b) slip length as a function of grafting density. (a) and (b) are extracted from molecular dynamic simulations. (c) Comparison of the renormalized relaxation times for films of thicknesses 65 and 39 nm is shown with respect to the expected scaling of renormalized bulk matrix viscosity. (d) Evolution of $\zeta = \frac{\tau_i/\tau_{473}}{\eta_i/\eta_{473}}$ as a function of temperature is shown for a composite film of thicknesses 65 nm (open squares) and 39 nm (open circles). The horizontal dashed-dotted line indicates the expected behavior, in the absence of interfacial effects on the dynamics of nanoparticles. Panels (a) and (b) are adapted from Ibrahim *et al.*[95] Panels (c) and (d) are adapted from Begam *et al.*[136]

viscosity, is significantly different from bulk viscosity. The presence of such interfacial layers with different viscosities is in line with the theoretical model of Servantine and Mueller.[138] In addition, the relaxation time had anomalous wavevector q dependence.[136] For instance, the relaxation times measured for films of thickness 39 nm revealed q independence, though the Brownian motion of nanoparticles is expected to result in $\tau \sim q^{-2}$. This suggests that these systems display strong length scale-dependent hydrodynamic interactions due to the presence of an interfacial layer with an interfacial slip. This is interesting as hydrodynamic interactions in polymer melts are expected to be screened within the size of a monomer.

4.7 Fragility of PNCs

The behaviour of glasses near T_g is still a mystery. The relationship between fast-increasing relaxation times and heterogeneous dynamics near T_g is not fully understood. There are various contradicting results in this field. Fragility is a key dynamical parameter used to understand the glass-forming ability of such materials.[19,161,162] The notion of fragility was proposed by Angell in 1980s,[163] to categorize glass formers into strong and fragile based on the variation of α relaxation time (τ_α) or viscosity η near T_g. Fragility measures how fast the variation in viscosity changes or alpha relaxation dynamics slows down near T_g when approached from $T > T_g$ *i.e.*,[70,164]

$$m = \left.\frac{\partial \log(\eta)}{\partial (T/T_g)}\right|_{T=T_g} \quad (42)$$

For polymer glasses, fragility depends on the strength of inter-particle interactions. A sharp slowing down of dynamics near glass transition temperature for PNCs with small nanoparticles (diameter $\approx$ 1.8 nm) as compared to conventional nanocomposites with particles of diameters 10–50 nm is reported by Cheng *et al.*[165] The study of the influence of C60 fullerenes on the fragility of PS[161] shows that the dynamic fragility of PS increases with C60 content in fresh samples and decreases in annealed PNCs due to agglomeration of fullerenes. Reduction in fragility by reducing the molecular weight of tethered chains is reported in PS-grafted silica nanoparticles.[166] The effect of polymer–nanoparticle interactions on the fragility of PNCs is investigated using equilibrium CGMD simulations by Starr and Douglas.[19] Simulations suggest that PNCs with non-attractive polymer–nanoparticle interactions are less fragile and those with attractive interactions are more fragile. However, the reduction in fragility with nanoparticle concentration for both attractive and nonattractive nanoparticle interactions is also reported.[167] Given this background, in the next section, we discuss work from our group, revealing how an interplay of the film–substrate interface and the PGNP–particle interface controls the viscosity and fragility of PNC thin films.[70]

4.7.1 Viscosity and fragility of PNC thin films: an interplay of two interfaces. The influence of polymer–substrate interactions on material properties has garnered significant attention. In particular, the presence of an interfacial layer with reduced polymer chain mobility has been shown to affect both viscosity and glass transition temperature, as demonstrated by numerous experimental studies.[168,169] In PNCs, higher NP density is found in this interface layer from XR studies and MD simulations.[54,55,57,70] In this scenario, here we focus on results obtained from XPCS measurements, probing the viscosity of PNC films, and CGMD simulations providing microscopic structural insights. To establish the role of ILs, we focused on two different values of $f = 0.06$ and $f = 0.4$. For highlighting the role of film confinement, we probed the microscopic dynamics of PNC films of four different thicknesses varying from 30 to 65 nm.

As depicted in Fig. 8a and b, in line with the discussions in Section 4.3, CGMD simulations reveal that the NP segregation in the interface layer decreases by increasing entropic compatibility between graft and matrix chains defined by the f parameter. The NP density profile extracted from the simulation studies shows a peak at the interface and the peak height decreases with increasing f (refer to Fig. 8c). XR experiments reveal that the thickness of this adsorbed layer h_{int} decreased with increasing film thickness h (Fig. 8d). Overall, in line with the literature on polymer films,[32] the viscosity of the PNC films increased systematically with increasing polymer–substrate interfacial layer thickness, h_{int}. Interestingly, for films with similar h_{int}, the particle–polymer IL played a decisive role in determining the absolute viscosity of the film (Fig. 8e). Upon comparing PNC films with similar h_{int}, films with higher f values (correspondingly larger ξ) displayed higher viscosity. This observation reveals the effect of the subtle interplay of two interfacial layer thicknesses (ξ and h_{int}) on the viscosity of PNC thin films. Similarly, interfacial entropic interactions are found to affect the fragility of polymer films under confinement. The PNC with a smaller ξ (smaller-f) exhibits an increase in fragility with increasing confinement (Fig. 8f). In contrast, both pristine PS and PNCs with a greater ζ (higher-f) become stronger glasses with confinement as measured by their fragility.

5 Interfacial entropic effect on temperature-dependent microscopic structural dynamics

Polymer and PNC melts are known to exhibit a hierarchy of length and time scales, especially showing a variety of relaxation spectra at different length scales. Polymer relaxation processes are typically categorized into three types: alpha-relaxation, beta-relaxation, and gamma-relaxation.[170] However, several studies[61,171] reveal an intermittent relaxation process that could not be classified into any of the above-mentioned relaxation categories. Upon comparing the measured relation spectra of polystyrene with alpha- and beta-relaxation spectra, Kanaya *et al.*[171] used the terminology fast and slow processes for the experimentally observed relaxation processes. The fast process is associated with the librational motion of phenyl rings of polystyrene, which is coupled with main chain motion

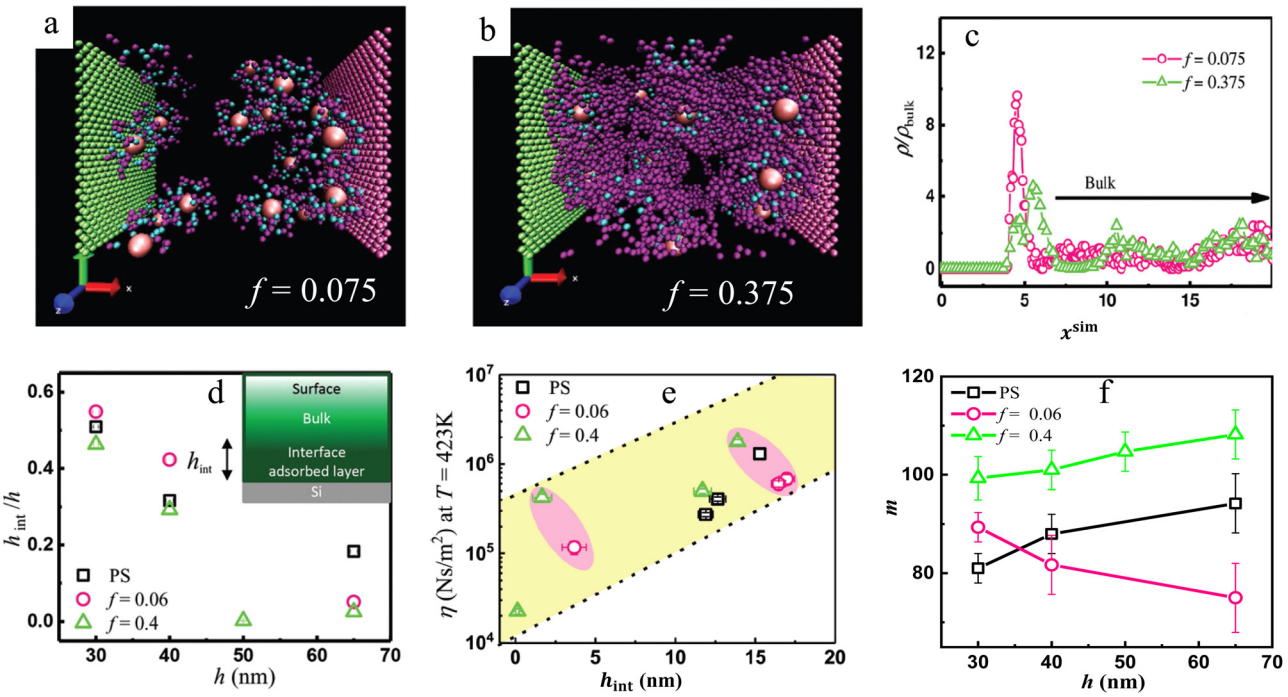

Fig. 8 Changes in substrate–polymer interfacial thickness, viscosity and fragility with confinement: snapshots of coarse-grained MD simulations, generated using visual molecular dynamics (VMD), of the PNC systems for (a) small-f (=0.075) and (b) high-f (=0.375). The system consists of PGNPs embedded in a matrix of pure PS chains confined between two walls (green and rose in colour). For clarity in display, matrix polymers are removed from the simulation system. (c) Normalized nanoparticle density profile (with respect to bulk density ρ_{bulk}) along the confinement direction x^{sim} estimated from the simulation. (d) Normalized adsorbed layer thickness h_{int} with respect to total thickness h for PS and PNC films with various thicknesses. Schematic of the film structure is shown in the inset. (e) Viscosity, η, at T = 423 K as a function of film-substrate IL, h_{int}, for all the PS and PNC films of various film thicknesses, h, from the experiment. The pink shaded regions indicate the scaling of η with f for approximately similar values of h_{int}. (f) Absolute values of fragility, m, as a function of thickness for pure PS and PNC films with different f values. All the plots are adapted from ref. 70.

near the glass transition temperature. Although the origin of the slow process is not clear, Kanaya *et al.*[171] hypothesised that the slow process is an elementary step of the conformational transition of the main chain.

While information on such processes for pure polymers is well established, our knowledge of equivalent features for PNCs remains incomplete. The enthalpic and entropic interactions between embedded nanoparticles (NPs) and polymer matrix chains may yield interesting deviations in the length and time scales corresponding to these ranges of microscopic dynamics. Based on this aspect, here we discuss the length-scale dependent dynamics observed in PNC melts utilizing quasi-elastic neutron scattering.[61]

For diffusive processes, the microscopic relaxation times τ are expected to follow q^{-2} scaling with the wave vector. For polymeric systems, the sub-diffusive motion of the segments results in $\tau \sim q^{-2/\beta}$, where β is the KWW exponent. This stronger dependence of τ is universal and observed for various polymers and glassformers.[172–174] Furthermore, a dynamical crossover from a scaling of $q^{-2/\beta}$ at low q to q^{-2} is observed at a critical wave vector q_c,[172,175] revealing the existence of a cut-off in length scales. Such crossover in q dependence also followed a transition from Gaussian to non-Gaussian dynamics (see ref. 176 and 177 for experiments and simulations on polyisoprene melts). As summarized in Fig. 9, Jhalaria *et al.*[175] reported the presence of similar behaviour in poly(methylacrylate) (PMA) grafted silica nanoparticles. Fig. 9a reveals that the τ of grafted polymers is less than the τ corresponding to ungrafted polymers. This indicates that a grafted chain experiences fewer local constraints than the corresponding pure polymer. Interestingly, q_c revealed a non-monotonic dependence with the molecular weight M_g of the grafted polymer (see Fig. 9(b)). In addition, the normalised segmental diffusivity shows a peak value around 61 kDa and these trends are similar to the nonmonotonic behaviour of the diffusion coefficient of CO_2 as depicted in Fig. 9(c). This nonmonotonic transport behaviour is explained as a thermodynamic consequence of the CPB-SDPB transition.[175]

Using QENS, we probed the effect of interfacial entropy, characterized by two different f values, on the microscopic dynamics of PS-grafted Au nanoparticle based bulk PNCs.[61] The results are summarized in Fig. 10. As depicted in Fig. 10(a), the τ of PNCs with larger f is smaller than that of the pure polymer. In contrast, τ of PNCs with smaller f is found to be larger than that of the neat polymer (Fig. 10(b)). Upon comparing our work with the literature[171,178,179] in Fig. 10(c), we find that the relaxation time extracted for PS and PNCs using QENS is probing complex fast dynamics (compared to alpha- and beta-relaxation). Similar to pure polymers[176,177] and pure PGNPs,[175] a length scale cut off q_c, which characterizes the

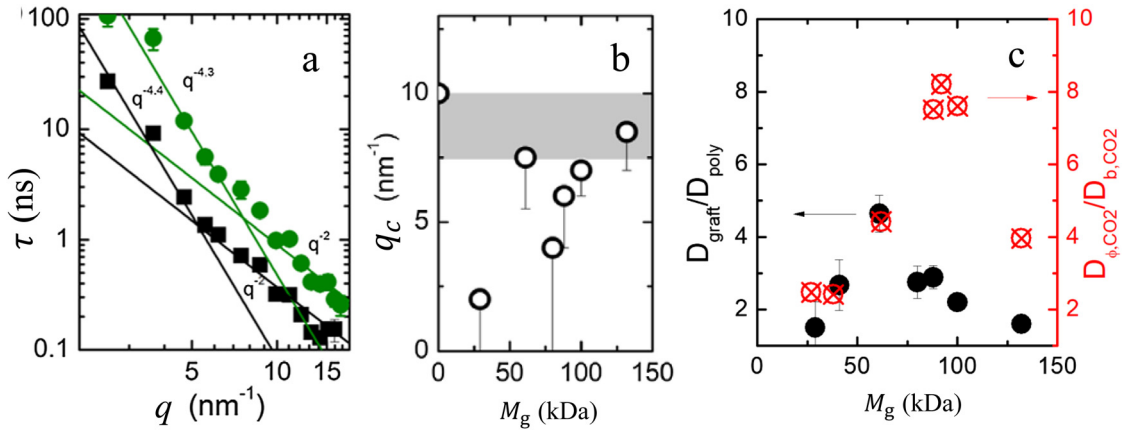

Fig. 9 Local dynamics and nonmonotonic behaviour as a function of graft molecular weight (M_g): (a) comparison of relaxation time for a composite with $M_g \approx 88$ kDa (black squares) and a bulk polymer with $M_g \approx 96$ kDa (green circles). (b) Crossover wave vectors (q_c) for grafted samples and the bulk polymer (gray band). (c) Normalized segmental diffusivity (black circles) and CO_2 diffusivity in PGNPs (red symbols) as functions of M_g, showing similar nonmonotonic trends with quantitative differences. The plots are adapted from ref. 175.

cross-over from Gaussian to non-Gaussian behaviour, is observed in PNC systems as well (small vertical lines in Fig. 10(a) and (b)). Furthermore, the absolute value of q_c depends on the temperature and f parameter.

A comparison of the cross-over wave vector q_c between PS and PNC systems reveals the intriguing entropic effect as depicted in Fig. 10(d). Clearly, the q_c of high-f samples is higher than that of all other samples, including their pure counterparts, at all temperatures. On the other hand, for low-f cases, q_c stays almost the same (until T = 410 K) or lower (T > 410 K) than that of the pure polymer. This reveals an intricate effect of entropic compatibility on the key dynamical features of PNCs. The q_c values of pure PGNPs are reported to be lower relative to neat polymers (Fig. 9(b)), indicating that locally diffusive

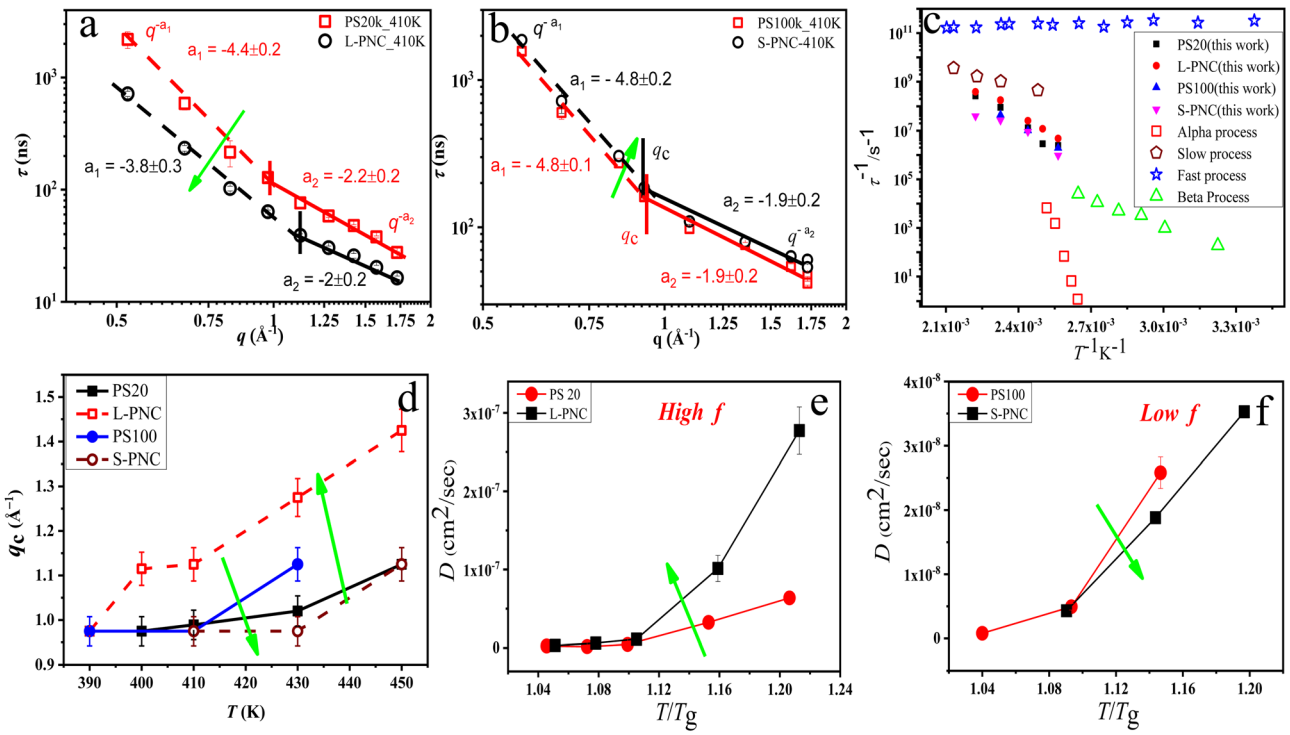

Fig. 10 Length-scale dependent microscopic dynamics of PS and PNCs: comparison of wavevector-dependent relaxation time (τ) for (a) L-PNCs (f = 0.225) and (b) S-PNCs (f = 0.03) with a pristine polymer at T = 410 K. (c) Comparison of temperature-dependent characteristic relaxation times in our work[61] with other dynamic processes in PS (measured using different techniques) extracted from the literature.[171,178,179] (d) Dynamical crossover wave vector (q_c) from Gaussian to non-Gaussian behavior as a function of temperature. Diffusion coefficient (D) as a function of temperature for (e) high-f and (f) low-f compared with the respective pure pristine systems. The plots are adapted from ref. 61.

dynamics are apparently persistent to larger length scales in the PGNPs.[175] To account for the cross-over of τ from $q^{-2/\beta}$ to q^{-2}, τ is modelled using a jump-diffusion model (JDM),[175,177,180,181] which considers the existence of an underlying distribution of jumps that give rise to the sub-diffusive regime at long times. The variation of τ with q is modeled using,

$$\tau(q) = \tau_0\left[1 + \left(\frac{1}{q^2 l_0^2}\right)\right]^{1/\beta} \quad (43)$$

where τ_0 is the time between successive jumps of most probable jump length l_0, which relates to the average distance a participating segment moves. Usually, there exists a distribution of jump lengths with l_0 representing the most probable value. Furthermore, a scaled polymeric diffusion constant can be estimated as

$$D = \frac{l_0^2}{\tau_0}. \quad (44)$$

The estimated values of τ_0 for PNCs were found to follow the same trend as that of τ, meaning that larger-f (smaller-f) samples have a smaller (larger) relaxation time compared to neat polymers. Furthermore, the normalized scaled diffusion of PMA-grafted nanoparticles showed a non-monotonic trend as a function of M_g as depicted in Fig. 9(c).[175] However, in PNCs, the scaled diffusion coefficient D of a lower f sample is higher than that of the neat polymer, whereas that of a higher f sample shows the opposite trend (Fig. 10(e) and (f)). These results indicate the intriguing effect of entropic compatibility on the length scale-dependent dynamics of PNCs.

6 Interfacial entropic effects on the properties of blends

Polymer blends combined with nanoparticles (NPs) are a new class of hybrid functional materials capable of exhibiting tunable novel physical properties.[182–184] However, the ability to control the dispersion state of NPs has been a challenge in the development of such materials for their wide range of applications.

Given this background, here we discuss our approach[182] harnessing the interfacial entropy at a particle–polymer interface in the thermodynamically demixing mixture of polymers – PS and PVME (poly(vinyl methyl ether)). As shown in Fig. 11, the PS and PVME mixture reveals a lower critical solution temperature (LCST) transition. We made films of 60/40 (w/w) ratio of PS and PVME containing PS-grafted gold nanoparticles. The mixture is coated on a silicon substrate. Due to low interfacial tension and preferential affinity, PVME wets both air–polymer and silicon–polymer interfaces and hence enriches the surface. Temperature modulated differential scanning calorimetry reveals variation in both T_g and its breadth in the presence of PS grafted gold nanoparticles (PS-*g*-nAu). High-magnification AFM images reveal the localization of PS-*g*-nAu on the PVME phase in the blend. The nanoparticle localization is shown in the phase diagram of the blend in Fig. 11. The expulsion of

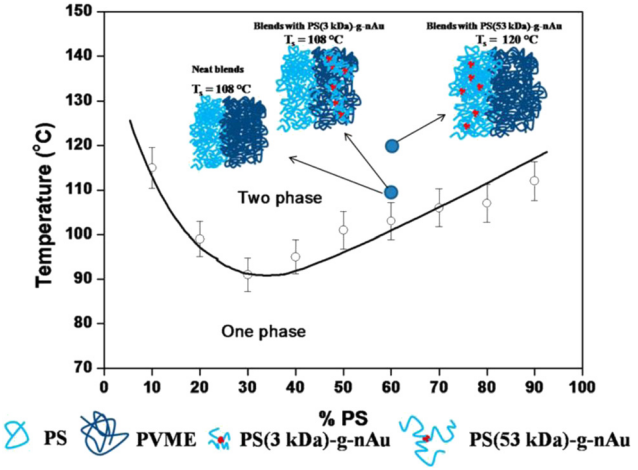

Fig. 11 Interfacial entropy allows controlling phase behavior of blends: phase diagram temperature T *vs.* weight fraction of PS, capturing the phase separation of PS-PVME. Also shown are schematics for demonstrating the localization of PGNPs in PS or PVME-rich regions controlled *via* M_g. The figure is adapted from Kar *et al.*[182]

PS-*g*-nAu from PS is driven purely by entropic interaction. Despite the PS coating over the gold core, the screening of the core with a short polymer chain is negligible. As a result, enthalpic interaction between PVME and the gold core leads to the localization of nanoparticles in the PVME phase. When the grafted chains are long, PS and nanoparticles experience an entropically favorable interaction producing well-dispersed nanoparticle states in the PS matrix. This result demonstrates that controlling the M_g allows the localization of particles in different domains in polymer blends.

So far we have demonstrated how harnessing the interfacial entropy allows us to control the dispersion of PGNPs, which, in turn, resulted in significant variations in the microscopic dynamics and in various properties and processing parameters including glass transition temperature, fragility and viscosity. In the next section, we highlight how such PGNPs allow accessing new parameter space in applications. While there are various application aspects, we do this by discussing the ability of PGNP membranes to enable efficient gas separation and water desalination.

7 Formation and understanding of PGNP membranes

Ultra-thin functional membranes made using nanoparticles show promise for a variety of uses, including gas and water filtration and flexible electronics and sensors.[185–191] These membranes are frequently composed of core–shell nanoparticles, and the degree of nanoparticle ordering and the softness and penetrability of the shell control the mechanical characteristics of these membranes. In this section, we discuss the formation of the PGNP membranes, and the effect of entropic compatibility on their thermal stability.

7.1 Preparation of PGNP membranes

PGNP membranes were prepared at the air/water interface in a Langmuir–Blodgett (LB) trough using the following steps.[59,60,192] Step 1: a homogeneous solution of PGNPs in chloroform was spread on the water surface using a Hamilton syringe. Due to unfavourable hydrophobic interactions between graft-polymer and water, the thin liquid film decomposes and forms a network of PGNP grains.[58,59,192] Step 2: using the Teflon barriers of the LB trough, the monolayer was compressed to obtain a thin dense membrane with a thickness below 10 nm. The typical surface pressure used is 35 mN m^{-1}. Step 3: this PGNP layer was transferred onto different hydrophobic substrates through the horizontal dipping (Langmuir–Schaefer) method. The AFM image of a transferred membrane is given in Fig. 12a. Step 4: these membranes were dried under vacuum for the complete removal of water.

7.2 Thermal stability of PGNP membranes

According to recent reports, under ambient circumstances, ultra-thin, freestanding membranes are found to have remarkable mechanical capabilities.[193] Nonetheless, in the majority of real-world uses, the membranes are supported by stable substrates and necessitate non-ambient functioning.[194] Therefore, it is important to investigate the function of contacts with the underlying substrates and the thermal stability of these ultra-thin nanoparticle-based membranes to fully realize their potential in a variety of applications and enhance their characteristics. Given this background, here we discuss how the thermal stability of PGNP membranes depends on the entropic interactions, defined by f, between the membrane and substrates.[59] We made PS grafted gold nanoparticle membranes on PS thin films of thickness $h \approx 80$ nm. We probed the temperature-dependent structure of the PGNP membranes in real space using AFM measurements and the penetration of the PGNPs into the films *via in situ* XR measurements.[59] The temperature-induced disordering of PGNP membranes on the PS thin film is summarized Fig. 12a–c. When heated above the T_g of both graft and matrix polymers, membranes lose their granular structure as individual PGNPs penetrate into the underlying polymer substrate as depicted in the schematic in Fig. 12d. Utilizing *in situ* XR, we show that during heating, penetration of PGNPs from the membrane layer to the substrate polymer layer is f-dependent, indicating the effect of entropic compatibility on facilitating fast PGNP penetration.[58] When the PGNP membrane is placed on chemically identical polymer substrates with different levels of entropic compatibility (defined by f), higher PGNP penetration (during heating) is observed at large f (Fig. 12e). As summarized in Fig. 12e, the temperature stability of the membranes increased

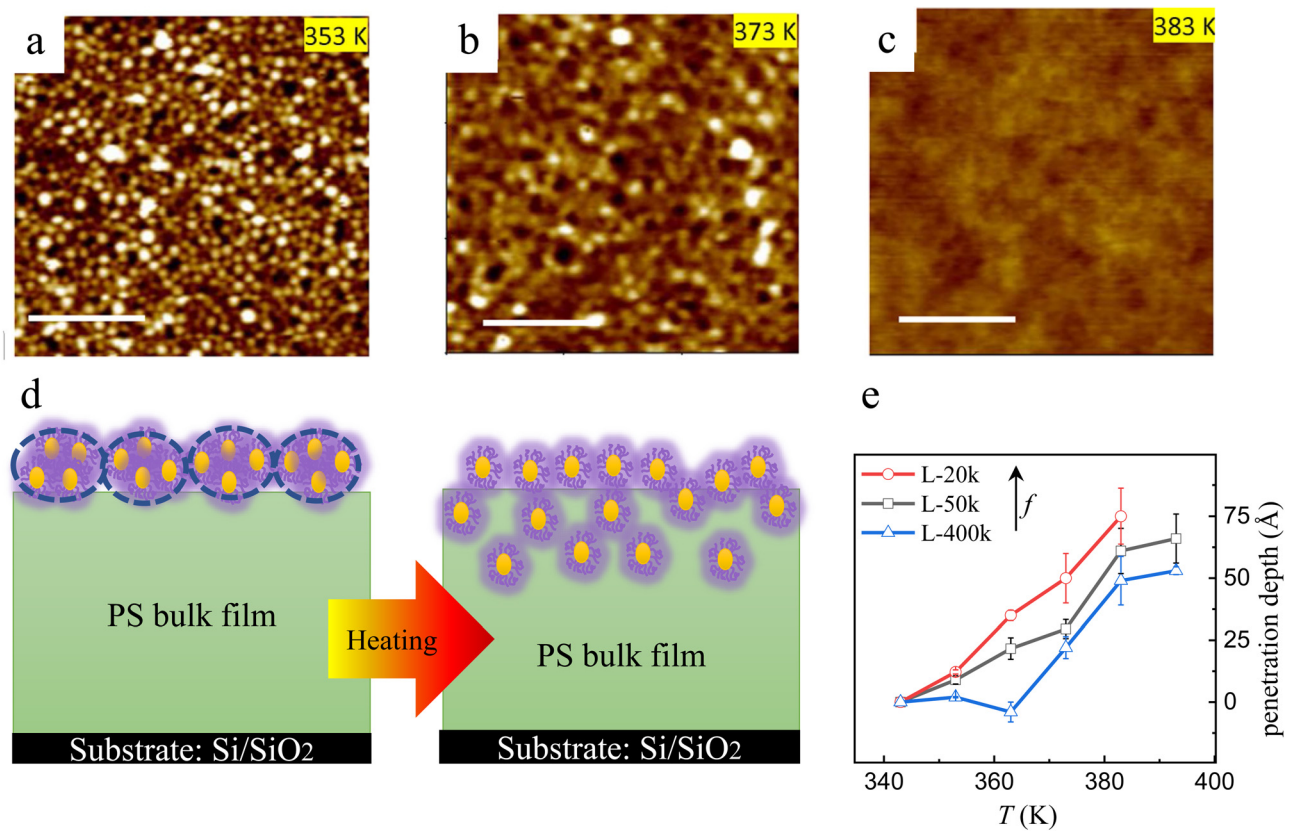

Fig. 12 Stability of the PGNP membrane: (a)–(c) AFM surface topography of the PGNP membrane on a PS substrate at different temperatures as mentioned in the legends (scale bar: 400 nm). (d) Schematic illustrating PGNP penetration into the PS bottom layer during heating. (e) The penetration depth of PGNPs into PS melts with varying f. The plots are adopted from ref. 58.

monotonously with a decrease in f, specifically by changing the molecular weight of the polymers comprising the substrate.[58,59]

7.3 Creation of high-density PNCs from PGNP membranes

The penetration of PGNPs, at high temperatures, into the polymer substrates provides a new lever to increase the loading fraction of PGNPs into polymer films. It is conceivable that the subsequent transfer and penetration of the membranes into the polymer substrates would yield an increase in the fraction of dispersed particles in the polymer matrices. This technique could be utilized as an effective tool to create PNCs with a high volume fraction of PGNPs. To utilize this approach, we need to understand the penetration kinetics of PGNPs into the substrates during heating and the interplay of different parameters such as particle size, softness, graft length, *etc.* Furthermore, nanoparticle penetration is important in various fields starting from targeted nanoparticle-based drug delivery to generating hybrid PNC materials.[195–197] By exploring the penetration of PS-grafted Au nanoparticles (PGNPs) into PS films, we show the formation of PNC layers close to the membrane–substrate film interface.[58,60] We followed the kinetics of penetration at different temperatures using *in situ* AFM.[60] The penetration of the PGNPs into polymer substrates results in a progressive decrease in the thickness of the membrane, as quantified in Fig. 13(a) and (b). By modelling the time-dependent decrease in the membrane height as an exponential with single relaxation time τ_p, we quantified the penetration time scales. Fig. 13c summarizes the temperature dependence of τ_p for systems with two different f values. Clearly, systems with higher entropic compatibility penetrate into the films at a rapid rate. Complementary CGMD simulations support the results as summarized in Fig. 12(d) and (e). These results highlight that f provides a new lever to control the stability of the membranes and the penetration kinetics. We believe these findings could be leveraged to create high-density PNCs that have potential in various membrane-related applications.

8 Applications: PGNP membranes for gas separation and water desalination

By harnessing interfacial entropy, we can design PNCs with tailored properties, making them highly effective for applications such as selective membranes for water desalination, and high-performance coatings. The ability to control interfacial entropy provides a powerful tool for engineering next-generation functional materials. Polymer membrane desalination technologies, like reverse osmosis (RO) and nanofiltration (NF), have advanced since the 1960s.[198] Membrane performance, often inversely correlated between water permeance and salt rejection, shows a tradeoff and possible upper bound.[191,199] Using water permeability and water/salt permeability selectivity for analysis reveals clearer trends. Selectivity is largely driven by diffusivity rather than solubility.

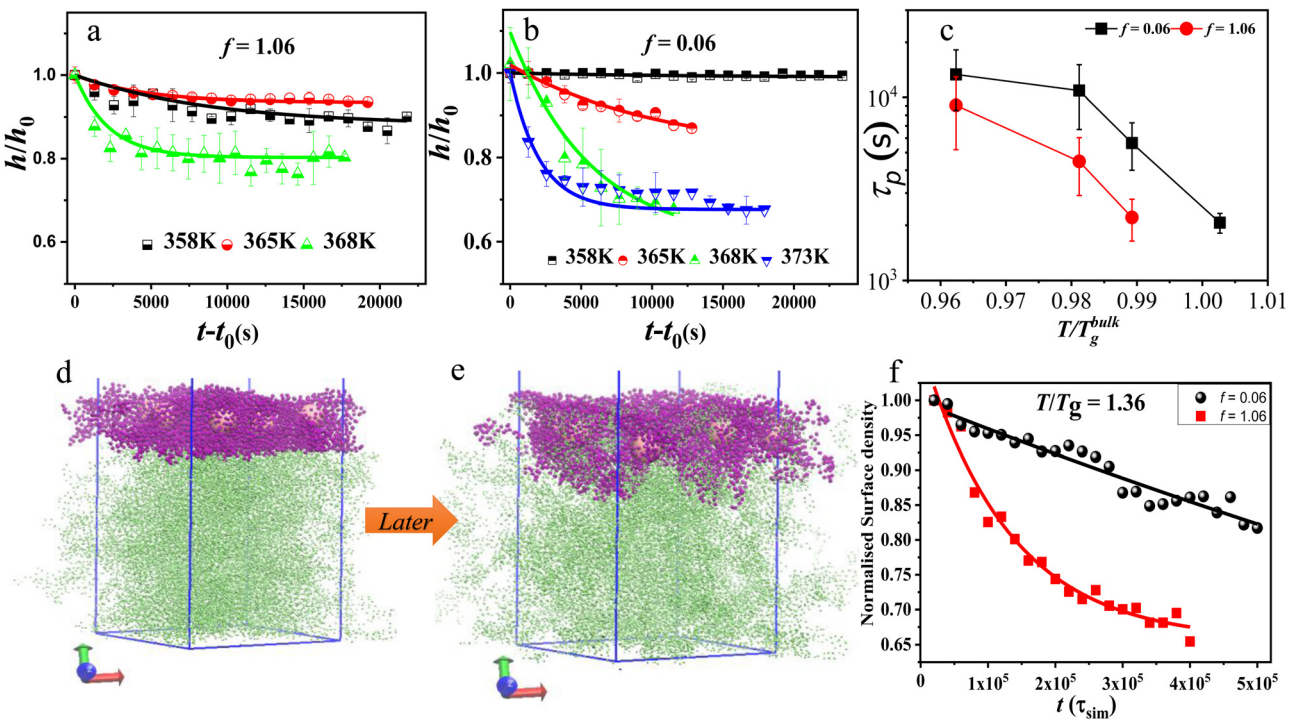

Fig. 13 Penetration kinetics of PGNPs into the substrate film at elevated temperatures: (a) decay of normalized height (h/h_0) as a function of waiting time (t/t_0) at temperatures near the respective (T_g) for f = 0.06 and f = 1.06. Data (symbols) are fitted with an exponential decay (solid lines). (b) Penetration time τ_p *vs.* (T/T_g) for PGNP–PS systems, highlighting differences between f = 0.06 and f = 1.06, controlled by entropic barriers. (c) MD simulations capture the entropic barrier effects. Representative snapshots of simulation boxes are shown for (d) f = 1.06 at ($t = 2 \times 10^4 \tau_{sim}$) and (e) f = 1.06 at $t = 2 \times 10^5 \tau_{sim}$. (f) Temporal evolution of the normalized surface density of PGNPs for the PGNP–PS system, adapted from ref. 60.

Water and salt transport in dense polymeric membranes follows the solution–diffusion mechanism, where small molecules first partition into the polymer matrix and then diffuse across it under a chemical potential gradient.[200,201] This process occurs within the free volume of amorphous regions, characterized by high chain mobility.[202,203] Studies have shown that modifying free volume properties, through changes in chain mobility or arrangement, influences the permselectivity of gas separation and ion-exchange membranes, which also operate *via* the solution–diffusion mechanism.[204,205] However, the impact of polymer structure on water and salt transport in desalination membranes remains insufficiently explored.[191]

Understanding this relationship is vital for designing membranes with enhanced selectivity, lower energy costs, and greater longevity. PGNPs have been extensively studied for gas separation, showing improvements that approach the upper bound curve. High-density ultrathin PGNP layers also demonstrate superior thermal and mechanical strength compared to conventional polymer membranes. These enhancements are attributed to the free volume effects and molecular variations in grafted chains[175,206–209] shown in Fig. 14. Bilchak *et al.*[206] reported that the free volume distribution of PGNPs can be tuned by adding free polymer chains. Adding short free chains, evenly distributed within the PGNP polymer layer, uniformly reduces gas permeability without significantly enhancing selectivity. In contrast, free chains of similar length to the grafts, which occupy interstitial spaces between PGNPs, selectively hinder larger gas molecules, boosting selectivity by up to two orders of magnitude with only moderate permeability loss for smaller gases. This finding highlights the potential to optimize GNP membranes for selective gas transport by leveraging entropic effects through tailored free polymer addition.[206] This work highlights the gas transport behaviour in polymer-grafted nanoparticle (PGNP) membranes, emphasizing the role of the interfacial layer in controlling permeability and selectivity. Fig. 14(A) presents a Robeson plot of CO_2/CH_4 separation, showing how GNP membranes surpass conventional polymers by manipulating free volume and interfacial interactions. The

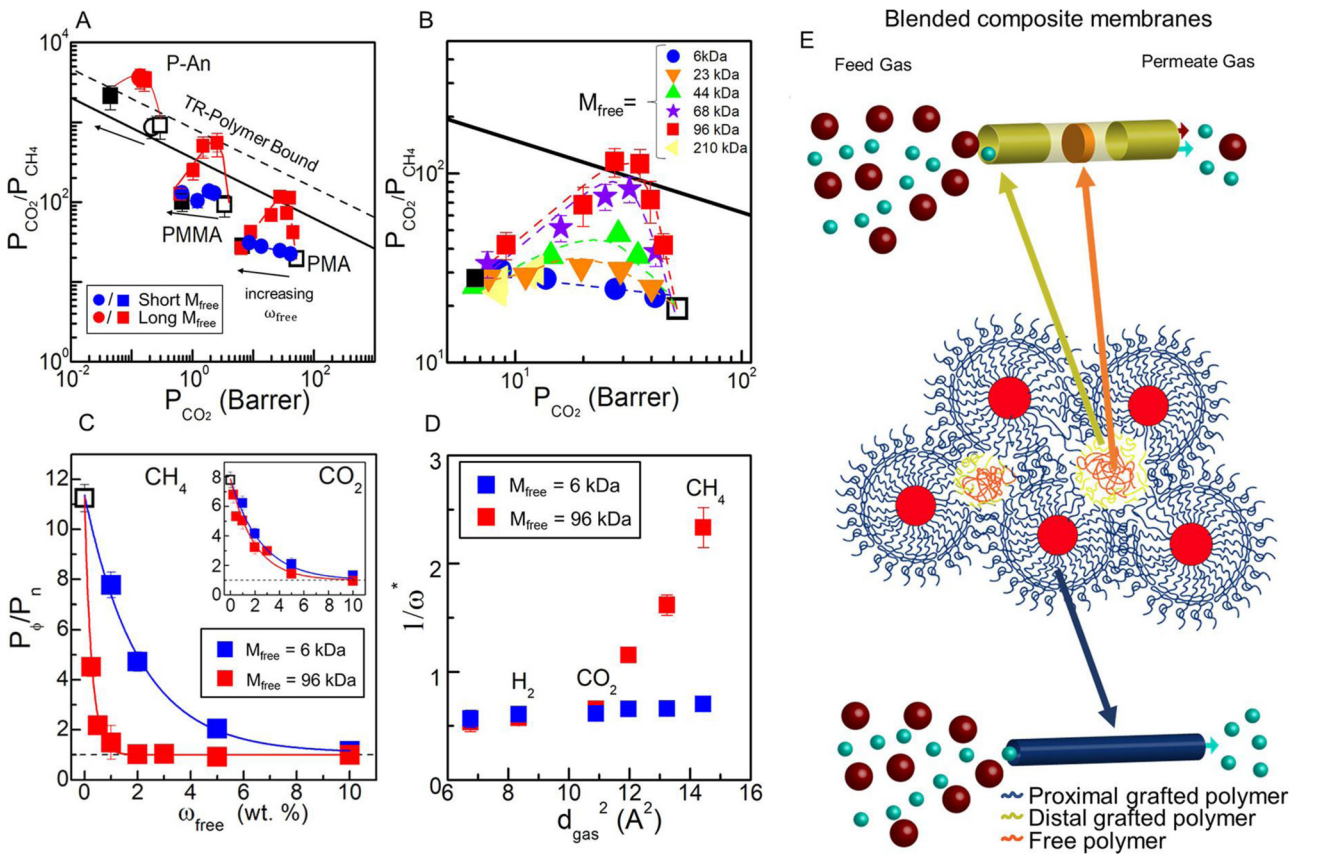

Fig. 14 Pure gas transport in PGNP/free chain mixtures: (A) CO_2/CH_4 Robeson plot of PMA- and PMMA-grafted nanoparticle (NP) membranes under similar conditions. PMA systems include $M_g \approx 100$ kDa with "short" ($M_{free} \approx 6$ kDa) and "long" ($M_{free} \approx 96$ kDa) free chains. PMMA systems include $M_g \approx 100$ kDa with "short" ($M_{free} \approx 3$ kDa) and "long" ($M_{free} \approx 90$ kDa) chains. PA_n-based composites ($M_g \approx 30$ kDa, $M_{free} \approx 30$ kDa) are also shown. The solid black line represents the 2008 Robeson upper bound. (B) CO_2/CH_4 selectivity enhancements in PMA–GNP composites ($M_g \approx 100$ kDa) with varying M_{free} and weight fractions. The neat PMA–GNP (open black square) shows maximum selectivity enhancement at $M_{free} \approx 96$ kDa. (C) CH_4 permeability enhancement in PMA–GNP composites with $M_{free} \approx 6$ kDa and $M_{free} \approx 96$ kDa at different ω_{free} values. Inset: CO_2 permeability enhancement. Solid lines represent model fits. (D) Critical ω values (ω^*) as a function of gas kinetic diameter (d_{gas}^2) in PMA-based composites for two M_{free} values. (E) Schematic illustration of gas transport in composite systems: longer free chains (M_{free}) segregate to distal regions, hindering larger gas molecules' transport while facilitating smaller molecule diffusion. The figure is adapted from ref. 206.

interfacial layer, formed by grafted polymer chains surrounding nanoparticles, creates a heterogeneous transport medium that enhances gas diffusion. Fig. 14(B) shows the effect of M_g on CO_2 permeability, where increased M_g initially enhances free volume and permeability but later leads to chain interpenetration and densification of the interfacial layer, reducing transport efficiency. Fig. 14(C) highlights the reduced aging effects in PMMA GNP membranes, attributed to the constrained motion of polymer chains in the interfacial region, which limits relaxation and densification over time. Fig. 14(D) presents CO_2 permeance and CO_2/CH_4 selectivity as a function of film thickness, showing that thin-film PGNP membranes maintain high performance due to the stabilizing effects of the interfacial layer. Finally, Fig. 14(E) provides a schematic of GNP membranes, where the interfacial layer creates free volume, particularly in the distal regions between nanoparticles, facilitating selective gas transport. Altogether, these figures provide a comprehensive understanding of how polymer grafting, interfacial layers, and nanoparticle structuring influence membrane performance, underpinned by fundamental polymer physics and free volume theory.

Inspired by the success of PGNP membranes in gas separation, we explored the applicability of membranes obtained *via* layer-by-layer assembly, using the Langmuir–Blodgett technique, in water desalination.[99] This would be beneficial as such frugal methods could effectively reduce the overall cost of clean water production. We modified polyamide (PA) membranes by coating multilayers of PGNP membranes as captured in the schematic shown in Fig. 15(a). Unlike most current studies focused on conventional surface treatments of PA membranes, this LB approach ensures complete surface coverage, thus paving new pathways for material development. We utilize the equations derived in the section on water desalination membranes to calculate key parameters such as J_w, A, R_s, and the A/B ratio from eqn (22)–(27), enabling a detailed analysis of membrane performance. We observed that the water permeance of these membranes scales inversely with their thickness when comprised of at least three nanoparticle (NP) layers (Fig. 15(b)). Notably, permeability exhibits a maximum performance for an intermediate M_g (refer Fig. 15(c) and (d)). Through osmotic compressibility measurements, we establish that these effects are driven by the non-monotonic relationship between membrane-free volume and M_g, consistent with findings based on gas permeability.[206] Given that solvent and solute transport mechanisms differ, our constructs provide independent parameters to control solvent permeance and permselectivity. This offers an alternative route for developing low-cost, energy-efficient water desalination membrane technologies. Additionally, our methodology can be extended to other membrane separation applications, including gas separation,

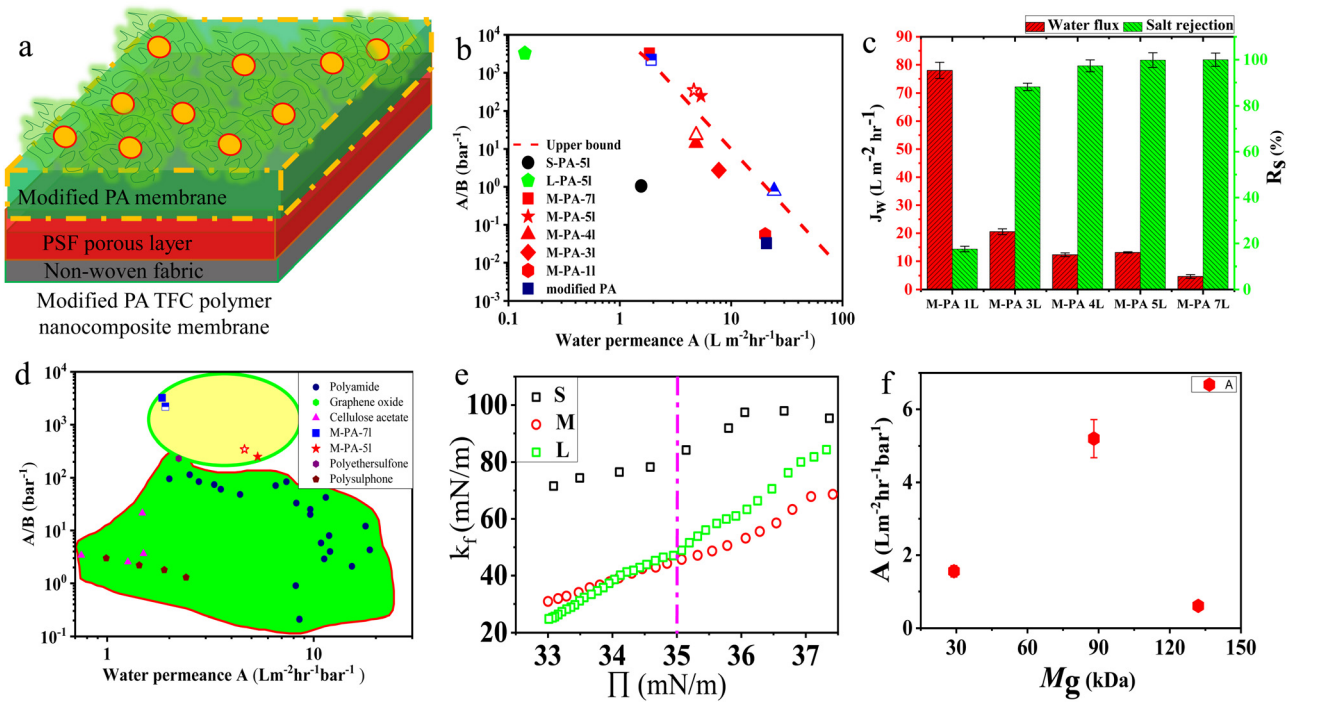

Fig. 15 Comparison and innovation in RO membranes: (a) schematic of membrane preparation-pristine PA-TFC to processed membranes with PGNP layers added *via* the Langmuir–Blodgett (LB) method. (b) Water perm-selectivity (A/B) *vs.* water permeance (A) for input pressures of 60 psi (closed symbols) and 75 psi (half-open symbols). Membranes with $N \geq 5$ and $N = 4$ at 75 psi exceed the empirical upper bound for RO membranes (dashed line). Tests were conducted with 2000 ppm NaCl at 25 °C and 60 psi. Higher transfer pressure (Π) improves A/B, indicating it as a key parameter alongside M_g, N, and input pressure. (c) Histogram of salt rejection (R_S) and water flux (J_w) for M-PA membranes with varying layer numbers (N). (d) Comparison plot of water perm-selectivity (A/B) *versus* water permeance (A) for various membrane types, highlighting the enhanced performance and novelty of the modified PA membrane with PGNP layers. (e) Dependence of κ_f on Π for Langmuir monolayers of all PGNPs. (f) Water permeance (A) of the PNC-modified PA membrane M_g, for $N = 5$ layers of PGNPs, adapted from ref. 99.

due to the versatility of the LB approach used in fabricating these PGNP multilayers.

As illustrated in Fig. 15(c), membranes with one NP layer exhibit water permeance comparable to that of the PA layer, likely due to layer imperfections (''pin holes''). In contrast, membranes exceeding three NP layers demonstrate a permeance that decreases inversely with PGNP membrane thickness, aligning with expectations from the solution diffusion model.[97,210] Furthermore, for membranes with five NP layers, permeance reaches a maximum near an average molecular weight (M_g) of approximately 88 kDa, echoing trends observed in gas permeability for similar materials Fig. 15(e). To understand the non-monotonicity, we probed the membrane compressibility characteristics, defined by κ_f (summarized in Fig. 15(e)). Careful examination of the curves for the three grafting molecular weights reveals that at Π = 35 mN m^{-1}, the compressibility factor (κ_f) is minimized for the M-PGNP configuration (Fig. 15(c)–(d)). From standard thermodynamic principles, κ_f is an inverse measure of density fluctuations and thus relates to available free volume. This indicates that among equally compact PGNP layers, as captured in Fig. 15(f), for a fixed number of layers, the permeance A exhibits a non-monotonic dependence on the graft molecular weight, peaking around a specific molecular weight. This behavior is ascribed to variations in free volume within the interfacial layer, as indicated by the osmotic compressibility modulus (κ_f). The lowest κ_f, which suggests maximal free volume and consequently higher water flux (J_w), is observed for the intermediate graft molecular weight. The lowest κ_f, indicating maximal free volume and thus higher water flux, is observed for the intermediate graft molecular weight. This finding aligns with previous studies on gas transport,[206,208] confirming that enhanced free volume facilitates solvent transport. This work summarizes that by tuning the M_g and layer thickness, membrane performance can be optimized, offering a strategy for improving water permeance while maintaining high selectivity in desalination applications.[99] The interplay between free volume and the emergent properties of membranes highlights their transformative potential as a design principle. This intrinsic property links the microscopic dynamics of glass-forming systems with macroscopic functionalities, enabling the rational tuning of membrane selectivity, permeability, and stability. By leveraging the principles of free volume, researchers can navigate the intricate physics of polymer dynamics to develop next-generation membranes for critical applications in gas separation, water purification, and beyond, underscoring the profound synergy between condensed matter physics and materials engineering.

9 Perspectives

In this review, we emphasize the pivotal role of the nanoparticle–polymer interface in defining the flow, thermal, mechanical, optical, and electrical properties of polymer PNCs. The interplay between enthalpic and entropic interactions at this interface fundamentally differentiates the behaviour of PNCs, particularly when comparing conventional composites to those based on PGNPs. The structure and properties of the interfacial layer (IL) in enthalpic PNCs are influenced primarily by NP–polymer interactions and the molecular weight of the matrix polymer. Conversely, in PGNP-based entropic PNCs, parameters such as the molecular weight ratio f, grafting density, and NP size dictate the IL properties, entropic interactions, and ultimately, the dispersion and performance of the composite material. A key insight is the ability to control the microscopic parameter ξ, representing matrix chain penetration depth, through variations in f. This parameter not only modulates the entropic interactions but also governs the dispersion state of PNCs, enabling tailored material properties. For entropic PNCs, the well-dispersed and stable composites achievable even at high particle fractions offer unique opportunities to enhance physical properties, such as glass transition temperature, viscosity, and dynamic heterogeneity. The versatility of the f-parameter, which can control chain penetration, underscores its central role in designing advanced PNC materials.

When applied to confined systems, such as thin films or coatings, the dynamics become more complex due to the presence of a second interface between the film and substrate. Notably, the dynamical properties of PNC thin films are influenced by the interplay between two critical interfaces: (a) the PGNP–polymer interface, characterized by ξ, and (b) the substrate–polymer interface, defined by the thickness of the adsorbed layer (h_{int}). These two parameters can be independently tuned through variations in grafted chain size and film processing conditions, offering a pathway to systematically modulate viscosity, fragility, and other dynamical properties under confinement.

In the domain of polymeric membranes for gas separation and water desalination, the chain penetration between the grafted polymer layers on adjacent PGNPs emerges as a decisive factor in controlling parameters like porosity and free volume, which plays a very important role in improving separation efficiency. The non-monotonic behaviour of gas separation efficiency observed in these systems highlights the intricate relationship between graft molecular weight and membrane free volume. Specifically, the inverse dependence of density fluctuations (κ_f) on free volume aligns with enhanced water flux (J_w) and selective gas permeability, providing novel insights into the design of energy-efficient separation technologies. By decoupling the transport mechanisms for solvents and solutes, PGNP membranes offer independent control over solvent permeance and permselectivity, paving the way for innovative, low-cost solutions in membrane applications.

Overall, this review illustrates how precise manipulation of NP–polymer interfaces, grafting parameters, and interfacial dynamics can enable transformative advances in PNC applications. The modular nature of these systems holds immense potential for breakthroughs in sustainability-focused technologies, including high-performance gas separation and water desalination membranes. Future investigations into the effects of graft chemistry, hydrophobicity, and density could further

deepen our understanding and drive the next generation of tailored nanocomposite materials.

Looking ahead, a key challenge is leveraging entropic effects at PGNPs interfaces to design materials with tailored properties. The discussions in this review focused on the equilibrium phase behaviour of polymer nanoparticle mixtures. However, polymers and polymer nanocomposites are often processed at rapid rates and elevated temperatures. Several experiments suggest that the subsequent quenching to lower temperatures may freeze polymers in non-equilibrium conditions.[211–213] Such nonequilibrated polymers display a rich range of structure formation processes and properties beyond the predictions of the equilibrium framework.[211–213] Furthermore, external fields like temperature (heating and cooling of composites) could introduce additional contributions to the free energy, thereby allowing the control of the dispersion of PGNPs. For instance, we revealed[57] that elevated temperatures enhance the dispersion of PGNPs in otherwise immiscible systems. Similarly, any dynamic changes invoking new contributions to free energy could allow the harnessing of the dispersion behaviour of PGNPs. Thus, efforts focusing on understanding the phase behaviour of nanoparticles in nonequilibrium conditions, involving processing and external fields, could provide new avenues to control the dispersion of particles in polymer matrices. This, in turn, could allow tuning the desired properties of PNCs in a controlled manner. On the other hand, phase separation phenomena, such as those in bicontinuous interfacially jammed emulsions (Bijels), offer opportunities to create interconnected networks with tunable mechanical and transport properties. The interplay between grafted polymer chains and the matrix introduces entropic constraints that influence phase behaviour and stability. By exploring how grafting density, molecular weight ratio, and nanoparticle size affect interfacial entropic interactions, researchers can develop PGNP-based materials with enhanced phase stability, hierarchical structures, and adaptive properties. Such advances could enable breakthroughs in energy storage, filtration, catalysis, and responsive coatings, while also deepening our understanding of polymer dynamics in confined environments.

Data availability

No primary research results, software or code have been included and no new data were generated or analysed as part of this review.

Conflicts of interest

There are no conflicts to declare.

Acknowledgements

The authors thank Venkat Padmanabhan (Materials Design and Discovery, Avery Dennison, 8080 Norton Parkway Mentor, Ohio 44060, USA) and Mohd Ibrahim (Technical University of Munich, Germany) for their contributions to molecular dynamics (MD) simulations. We also extend our gratitude to Suryasarathi Bose (Department of Materials Engineering, Indian Institute of Science, Bangalore, India), Sanat K. Kumar (Department of Chemical Engineering, Columbia University, New York, USA), Brian C. Benicewicz (Department of Chemistry and Biochemistry, University of South Carolina, Columbia, SC, USA), Michael Sprung (Deutsches Elektronen-Synchrotron, Hamburg, Germany) and Victoria García Sakai (ISIS Neutron and Muon Source, Rutherford Appleton Laboratory, Chilton, Oxfordshire OX11 0QX, UK) for their valuable suggestions, experimental data collection and analysis guidance, and insightful discussions. S. C. acknowledges funding from the Kotak School of Sustainability (KSS), IIT Kanpur *via* DORA/2023508C.

Notes and references

1 S. K. Kumar, B. C. Benicewicz, R. A. Vaia and K. I. Winey, *Macromolecules*, 2017, **50**, 714–731.
2 P. F. Green, *Soft Matter*, 2011, **7**, 7914–7926.
3 Z. Zhang, N. Marioni, H. S. Sachar and V. Ganesan, *ACS Macro Lett.*, 2023, **12**, 1351–1357.
4 P. Akcora, S. K. Kumar, J. Moll, S. Lewis, L. S. Schadler, Y. Li, B. C. Benicewicz, A. Sandy, S. Narayanan and J. Ilavsky, *et al.*, *Macromolecules*, 2010, **43**, 1003–1010.
5 S. Y. Kim and C. F. Zukoski, *Soft Matter*, 2012, **8**, 1801–1810.
6 A. Milchev, S. A. Egorov, D. A. Vega, K. Binder and A. Nikoubashman, *Macromolecules*, 2018, **51**, 2002–2016.
7 B. Cappella and D. Silbernagl, *Thin Solid Films*, 2008, **516**, 1952–1960.
8 M. R. Bockstaller and E. L. Thomas, *J. Phys. Chem. B*, 2003, **107**, 10017–10024.
9 A. P. Holt, V. Bocharova, S. Cheng, A. M. Kisliuk, B. T. White, T. Saito, D. Uhrig, J. P. Mahalik, R. Kumar and A. E. Imel, *et al.*, *ACS Nano*, 2016, **10**, 6843–6852.
10 C.-C. Lin, P. J. Griffin, H. Chao, M. J. Hore, K. Ohno, N. Clarke, R. A. Riggleman, K. I. Winey and R. J. Composto, *J. Chem. Phys.*, 2017, **146**, 203332.
11 P. Choudhury, S. Dinda and P. K. Das, *Soft Matter*, 2020, **16**, 27–53.
12 M. Zafar, S. M. Imran, I. Iqbal, M. Azeem, S. Chaudhary, S. Ahmad and W. Y. Kim, *Results Phys.*, 2024, 107655.
13 J. Jancar, J. F. Douglas, F. W. Starr, S. Kumar, P. Cassagnau, A. Lesser, S. S. Sternstein and M. Buehler, *Polymer*, 2010, **51**, 3321–3343.
14 A. C. Balazs, T. Emrick and T. P. Russell, *Science*, 2006, **314**, 1107–1110.
15 L. M. Hall, B. J. Anderson, C. F. Zukoski and K. S. Schweizer, *Macromolecules*, 2009, **42**, 8435–8442.
16 T. B. Martin, P. M. Dodd and A. Jayaraman, *Phys. Rev. Lett.*, 2013, **110**, 018301.
17 S. T. Gobena and A. D. Woldeyonnes, *Discover Mater.*, 2024, **4**, 52.

18 H. Jamil, M. Faizan, M. Adeel, T. Jesionowski, G. Boczkaj and A. Balčiūnaitė, *Molecules*, 2024, **29**, 1267.
19 F. W. Starr and J. F. Douglas, *Phys. Rev. Lett.*, 2011, **106**, 115702.
20 A. Bansal, H. Yang, C. Li, B. C. Benicewicz, S. K. Kumar and L. S. Schadler, *J. Polym. Sci., Part B: Polym. Phys.*, 2006, **44**, 2944–2950.
21 S. K. Kumar and R. Krishnamoorti, *Ann. Rev. Chem. Biomol. Eng.*, 2010, **1**, 37–58.
22 M. E. Mackay, A. Tuteja, P. M. Duxbury, C. J. Hawker, B. Van Horn, Z. Guan, G. Chen and R. Krishnan, *Science*, 2006, **311**, 1740–1743.
23 R. Teijido, L. Ruiz-Rubio, A. G. Echaide, J. L. Vilas-Vilela, S. Lanceros-Mendez and Q. Zhang, *Prog. Org. Coat.*, 2022, **163**, 106684.
24 H. D. Wagner and R. A. Vaia, *Mater. Today*, 2004, **7**, 38–42.
25 S. C. Tjong, *Mater. Sci. Eng., R*, 2006, **53**, 73–197.
26 S. Sharma, P. Sudhakara, A. A. B. Omran, J. Singh and R. Ilyas, *Polymers*, 2021, **13**, 2898.
27 S. Ghosh and J. F. Douglas, *J. Chem. Phys.*, 2024, **160**, 104903.
28 R. A. Riggleman, G. Toepperwein, G. J. Papakonstantopoulos, J.-L. Barrat and J. J. de Pablo, *J. Chem. Phys.*, 2009, **130**, 244903.
29 M. Z. Rong, M. Q. Zhang and W. H. Ruan, *Mater. Sci. Technol.*, 2006, **22**, 787–796.
30 M. A. Ashraf, W. Peng, Y. Zare and K. Y. Rhee, *Nanoscale Res. Lett.*, 2018, **13**, 1–7.
31 Y. Yang, H. Tian, S. Napolitano and B. Zuo, *Prog. Polym. Sci.*, 2023, **144**, 101725.
32 S. Napolitano, *Soft Matter*, 2020, **16**, 5348–5365.
33 S. K. Kumar, N. Jouault, B. Benicewicz and T. Neely, *Macromolecules*, 2013, **46**, 3199–3214.
34 J. Liu, L. Zhang, D. Cao and W. Wang, *Phys. Chem. Chem. Phys.*, 2009, **11**, 11365–11384.
35 X. Zhang, X. Yan, Q. He, H. Wei, J. Long, J. Guo, H. Gu, J. Yu, J. Liu and D. Ding, *et al.*, *ACS Appl. Mater. Interfaces*, 2015, **7**, 6125–6138.
36 P. Akcora, H. Liu, S. K. Kumar, J. Moll, Y. Li, B. C. Benicewicz, L. S. Schadler, D. Acehan, A. Z. Panagiotopoulos and V. Pryamitsyn, *et al.*, *Nat. Mater.*, 2009, **8**, 354–359.
37 M. Willinger and E. Reimhult, *J. Phys. Chem. B*, 2021, **125**, 7009–7023.
38 M. A. Sattar, *ChemistrySelect*, 2021, **6**, 5068–5096.
39 S. Bhadauriya, X. Wang, A. Nallapaneni, A. Masud, Z. Wang, J. Lee, M. R. Bockstaller, A. M. Al-Enizi, C. H. Camp Jr and C. M. Stafford, *et al.*, *Nano Lett.*, 2021, **21**, 1274–1281.
40 Y. Sui, Y. Cui, X. Meng and Q. Zhou, *J. Appl. Polym. Sci.*, 2022, **139**, 52096.
41 A. Swain, N. Das A, N. Begam, A. Bhattacharyya, J. Basu, S. Chandran and M. Sprung, APS March Meeting Abstracts, 2021, pp. Y63–008.
42 S. Chandran, N. Begam and J. K. Basu, *J. Appl. Phys.*, 2014, **116**, 222203.
43 M. Ibrahim, N. Begam, V. Padmanabhan and J. Basu, *Soft Matter*, 2018, **14**, 6076–6082.
44 X. Dai, C. Hou, Z. Xu, Y. Yang, G. Zhu, P. Chen, Z. Huang and L.-T. Yan, *Entropy*, 2019, **21**, 186.
45 G. G. Vogiatzis and D. N. Theodorou, *Arch. Comput. Methods Eng.*, 2018, **25**, 591–645.
46 T. V. Ndoro, E. Voyiatzis, A. Ghanbari, D. N. Theodorou, M. C. Böhm and F. Müller-Plathe, *Macromolecules*, 2011, **44**, 2316–2327.
47 A. Tuteja, P. M. Duxbury and M. E. Mackay, *Phys. Rev. Lett.*, 2008, **100**, 077801.
48 D. Dukes, Y. Li, S. Lewis, B. Benicewicz, L. Schadler and S. K. Kumar, *Macromolecules*, 2010, **43**, 1564–1570.
49 R. Zhang, B. Lee, C. M. Stafford, J. F. Douglas, A. V. Dobrynin, M. R. Bockstaller and A. Karim, *Proc. Natl. Acad. Sci. U. S. A.*, 2017, **114**, 2462–2467.
50 A. J. Chancellor, B. T. Seymour and B. Zhao, *Anal. Chem.*, 2019, **91**, 6391–6402.
51 N. Tsubokawa, *Polym. J.*, 2007, **39**, 983–1000.
52 B. V. Tawade, M. Singh, I. E. Apata, J. Veerasamy, N. Pradhan, A. Karim, J. F. Douglas and D. Raghavan, *JACS Au*, 2023, **3**, 1365–1375.
53 C. K. Yee, R. Jordan, A. Ulman, H. White, A. King, M. Rafailovich and J. Sokolov, *Langmuir*, 1999, **15**, 3486–3491.
54 S. Chandran, N. Begam, V. Padmanabhan and J. K. Basu, *Nat. Commun.*, 2014, **5**, 3697.
55 S. Chandran, J. K. Basu and M. K. Mukhopadhyay, *J. Chem. Phys.*, 2013, **138**, 014902.
56 S. Chandran and J. K. Basu, *Eur. Phys. J. E: Soft Matter Biol. Phys.*, 2011, **34**, 1–5.
57 N. Begam, S. Chandran, N. Biswas and J. K. Basu, *Soft Matter*, 2015, **11**, 1165–1173.
58 N. A. Das, A. Swain, N. Begam, A. Bhattacharyya and J. K. Basu, *Macromolecules*, 2020, **53**, 8674–8682.
59 N. Das, N. Begam, S. Chandran, A. Swain, M. Sprung and J. K. Basu, *Soft Matter*, 2020, **16**, 1117–1124.
60 A. Swain, N. A. Das, S. Chandran and J. K. Basu, *Soft Matter*, 2022, **18**, 1005–1012.
61 A. Swain, N. Das, V. G. Sakai and J. K. Basu, *Soft Matter*, 2023, **19**, 5396–5404.
62 S. Minko, *Polymer Surfaces and Interfaces*, Springer, 2008, pp. 215–234.
63 J. Wong, C. J. Barrett and L. Reven, *Langmuir*, 2025, **41**, 5782–5793.
64 A. L. Mohamed, M. E. El-Naggar and A. G. Hassabo, *J. Mater. Res. Technol.*, 2021, **12**, 542–554.
65 M. Tolan and M. Tolan, *X-ray scattering from soft-matter thin films: materials science and basic research*, Springer, 1999, vol. 148.
66 J. Daillant and A. Gibaud, *X-ray and neutron reflectivity: principles and applications*, Springer, 2008, vol. 770.
67 S. K. Sinha, Z. Jiang and L. B. Lurio, *Adv. Mater.*, 2014, **26**, 7764–7785.
68 G. Grübel and F. Zontone, *J. Alloys Compd.*, 2004, **362**, 3–11.

69 F. Lehmkühler, W. Roseker and G. Grübel, *Appl. Sci.*, 2021, **11**, 6179.
70 N. Das, N. Begam, M. Ibrahim, S. Chandran, V. Padmanabhan, M. Sprung and J. K. Basu, *Nanoscale*, 2019, **11**, 8546–8553.
71 A. Madsen, R. L. Leheny, H. Guo, M. Sprung and O. Czakkel, *New J. Phys.*, 2010, **12**, 055001.
72 L. B. Lurio, G. M. Thurston, Q. Zhang, S. Narayanan and E. M. Dufresne, *Synchrotron Radiat.*, 2021, **28**, 490–498.
73 J. Song, Q. Zhang, F. de Quesada, M. H. Rizvi, J. B. Tracy, J. Ilavsky, S. Narayanan, E. Del Gado, R. L. Leheny and N. Holten-Andersen, *et al.*, *Proc. Natl. Acad. Sci. U. S. A.*, 2022, **119**, e2201566119.
74 Q. Berrod, K. Lagrené, J. Ollivier and J.-M. Zanotti, *Z. Phys. Chem.*, 2010, **224**, 5–32.
75 J. P. Embs, F. Juranyi and R. Hempelmann, *Z. Phys. Chem.*, 2010, **224**, 5–32.
76 K. Aomura, Y. Yasuda, T. Yamada, T. Sakai and K. Mayumi, *Soft Matter*, 2023, **19**, 147–152.
77 J. Colmenero and A. Arbe, *J. Polym. Sci., Part B: Polym. Phys.*, 2013, **51**, 87–113.
78 E. J. Bailey and K. I. Winey, *Prog. Polym. Sci.*, 2020, **105**, 101242.
79 N. C. Osti, N. H. Jalarvo and E. Mamontov, *Mater. Horiz.*, 2024, **11**, 4535–4572.
80 J. R. D. Copley and T. J. Udovic, *J. Res. Natl. Inst. Stand. Technol.*, 1993, **98**, 71.
81 M. Bée, *Chem. Phys.*, 2003, **292**, 121–141.
82 D. Tranchida, Z. Kiflie, S. Acierno and S. Piccarolo, *Meas. Sci. Technol.*, 2009, **20**, 095702.
83 G. Stan and S. W. King, *J. Vac. Sci. Technol., B: Nanotechnol. Microelectron.: Mater., Process., Meas., Phenom.*, 2020, **38**, 060801.
84 J. R. Withers and D. E. Aston, *Adv. Colloid Interface Sci.*, 2006, **120**, 57–67.
85 E. Finot, A. Passian and T. Thundat, *Sensors*, 2008, **8**, 3497–3541.
86 Y. M. Efremov, T. Okajima and A. Raman, *Soft Matter*, 2020, **16**, 64–81.
87 A. Swain, N. Begam, S. Chandran, M. Bobji and J. K. Basu, *Soft Matter*, 2020, **16**, 4065–4073.
88 B. Capella, P. Baschieri, C. Frediani, P. Miccoli and C. Ascoli, *IEEE Eng. Med. Biol. Mag.*, 1997, **16**, 58–65.
89 H.-J. Butt, B. Cappella and M. Kappl, *Surf. Sci. Rep.*, 2005, **59**, 1–152.
90 O. Pitois, P. Moucheront and X. Chateau, *J. Colloid Interface Sci.*, 2000, **231**, 26–31.
91 S. Cai and B. Bhushan, *Nanotechnology*, 2007, **18**, 465704.
92 H. Kim, A. Rühm, L. B. Lurio, J. K. Basu, J. Lal, D. Lumma, S. G. J. Mochrie and S. K. Sinha, *Phys. Rev. Lett.*, 2003, **90**, 068302.
93 D. J. Plazek and V. M. O'Rourke, *J. Polym. Sci., Part A-2*, 1971, **9**, 209–243.
94 C. Li, T. Koga, C. Li, J. Jiang, S. Sharma, S. Narayanan, L. B. Lurio, X. Hu, X. Jiao, S. K. Sinha, S. Billet, D. Sosnowik, H. Kim, J. C. Sokolov and M. H. Rafailovich, *Macromolecules*, 2005, **38**, 5144–5151.
95 M. Ibrahim, N. Begam, V. Padmanabhan and J. K. Basu, *Soft Matter*, 2018, **14**, 6076–6082.
96 L. Wang, T. Cao, J. E. Dykstra, S. Porada, P. Biesheuvel and M. Elimelech, *Environ. Sci. Technol.*, 2021, **55**, 16665–16675.
97 J. G. Wijmans and R. W. Baker, *J. Membr. Sci.*, 1995, **107**, 1–21.
98 J. G. Wijmans and R. W. Baker, *Mater. Sci. Membr. Gas Vap. Sep.*, 2006, **1**, 159–189.
99 A. Swain, S. Adarsh, A. Biswas, S. Bose, B. C. Benicewicz, S. K. Kumar and J. K. Basu, *Nanoscale*, 2023, **15**, 11935–11944.
100 M. R. Begley, D. S. Gianola and T. R. Ray, *Science*, 2019, **364**, eaav4299.
101 A. Jayaraman, *J. Polym. Sci., Part B: Polym. Phys.*, 2013, **51**, 524–534.
102 J. C. Foster, S. C. Radzinski and J. B. Matson, *J. Polym. Sci., Part A: Polym. Chem.*, 2017, **55**, 2865–2876.
103 F. L. Verso, L. Yelash, S. A. Egorov and K. Binder, *J. Chem. Phys.*, 2011, **135**, 244701.
104 M. J. A. Hore, L. T. J. Korley and S. K. Kumar, *J. Appl. Phys.*, 2020, **128**, 030401.
105 H. He, X. Shen and Z. Nie, *Prog. Polym. Sci.*, 2023, 101710.
106 W. Wu, M. Singh, A. Masud, X. Wang, A. Nallapaneni, Z. Xiao, Y. Zhai, Z. Wang, T. Terlier and M. Bleuel, *et al.*, *ACS Nano*, 2021, **15**, 12042–12056.
107 C. N. Likos, *Soft Matter*, 2006, **2**, 478–498.
108 C. Likos, H. Löwen, M. Watzlawek, B. Abbas, O. Jucknischke, J. Allgaier and D. Richter, *Phys. Rev. Lett.*, 1998, **80**, 4450.
109 C. N. Likos, *Phys. Rep.*, 2001, **348**, 267–439.
110 Ł. Baran and S. Sokołowski, *J. Chem. Phys.*, 2017, **147**, 044903.
111 W. Wu, W. Wang and J. Li, *Prog. Polym. Sci.*, 2015, **46**, 55–85.
112 P. A. Tikhonov, N. G. Vasilenko and A. M. Muzafarov, *Dokl. Chem.*, 2021, 1–17.
113 D. Vlassopoulos, G. Fytas, T. Pakula and J. Roovers, *J. Phys.: Condens. Matter*, 2001, **13**, R855.
114 J. M. Ren, T. G. McKenzie, Q. Fu, E. H. Wong, J. Xu, Z. An, S. Shanmugam, T. P. Davis, C. Boyer and G. G. Qiao, *Chem. Rev.*, 2016, **116**, 6743–6836.
115 S. Srivastava, S. Chandran, A. K. Kandar, C. K. Sarika, J. K. Basu, S. Narayanan and A. Sandy, *J. Chem. Phys.*, 2010, **133**, 151105.
116 L. R. Hutchings and R. W. Richards, *Macromolecules*, 1999, **32**, 880–891.
117 M. Daoud and J. P. Cotton, *J. Phys.*, 1982, **43**, 531–538.
118 J. K. Basu, J. C. Boulliard, B. Capelle, J. Daillant, P. Guenoun, J. W. Mays and J. Yang, *Macromolecules*, 2007, **40**, 6333–6339.
119 J. D. Thomin, P. Keblinski and S. K. Kumar, *Macromolecules*, 2008, **41**, 5988–5991.
120 D. Sunday, J. Ilavsky and D. L. Green, *Macromolecules*, 2012, **45**, 4007–4011.
121 Y. Wang, J. Chen, C. Zhu, B. Zhu, S. Jeong, Y. Yi, Y. Liu, J. Fiadorwu, P. He and X. Ye, *Nano Lett.*, 2021, **21**, 5053–5059.

122 I. Borukhov and L. Leibler, *Macromolecules*, 2002, **35**, 5171–5182.
123 P. G. Ferreira, A. Ajdari and L. Leibler, *Macromolecules*, 1998, **31**, 3994–4003.
124 A. Arceo, L. Meli and P. F. Green, *Nano Lett.*, 2008, **8**, 2271–2276.
125 A. Bansal, H. Yang, C. Li, K. Cho, B. C. Benicewicz, S. K. Kumar and L. S. Schadler, *Nat. Mater.*, 2005, **4**, 693–698.
126 D. M. Trombly and V. Ganesan, *J. Chem. Phys.*, 2010, **133**, 154904.
127 B. Natarajan, T. Neely, A. Rungta, B. C. Benicewicz and L. S. Schadler, *Macromolecules*, 2013, **46**, 4909–4918.
128 A. Hariharan, S. K. Kumar, M. H. Rafailovich, J. Sokolov, X. Zheng, D. Duong, S. A. Schwarz and T. P. Russell, *J. Chem. Phys.*, 1993, **99**, 656–663.
129 D. Cangialosi, A. Alegria and J. Colmenero, *Prog. Polym. Sci.*, 2016, **54**, 128–147.
130 L. Berthier and G. Biroli, *Rev. Mod. Phys.*, 2011, **83**, 587–645.
131 G. B. McKenna and S. L. Simon, *Macromolecules*, 2017, **50**, 6333–6361.
132 F. Ondreas, P. Lepcio, M. Zboncak, K. Zarybnicka, L. E. Govaert and J. Jancar, *Macromolecules*, 2019, **52**, 6250–6259.
133 A. Ghanekarade, A. D. Phan, K. S. Schweizer and D. S. Simmons, *Proc. Natl. Acad. Sci. U. S. A.*, 2021, **118**, e2104398118.
134 S. Y. Kim, H. W. Meyer, K. Saalwaächter and C. F. Zukoski, *Macromolecules*, 2012, **45**, 4225–4237.
135 J. T. Kalathi, G. S. Grest and S. K. Kumar, *Phys. Rev. Lett.*, 2012, **109**, 198301.
136 N. Begam, S. Chandran, M. Sprung and J. K. Basu, *Macromolecules*, 2015, **48**, 6646–6651.
137 G. Batchelor, *J. Fluid Mech.*, 1976, **74**, 1–29.
138 J. Servantie and M. Müller, *Phys. Rev. Lett.*, 2008, **101**, 026101.
139 M. E. Mackay, T. T. Dao, A. Tuteja, D. L. Ho, B. Van Horn, H.-C. Kim and C. J. Hawker, *Nat. Mater.*, 2003, **2**, 762–766.
140 M. Wang and R. J. Hill, *Soft Matter*, 2009, **5**, 3940–3953.
141 E. Senses, C. L. Kitchens and A. Faraone, *J. Polym. Sci.*, 2022, **60**, 1130–1150.
142 K. Nusser, G. J. Schneider, W. Pyckhout-Hintzen and D. Richter, *Macromolecules*, 2011, **44**, 7820–7830.
143 G. K. Batchelor, *J. Fluid Mech.*, 1970, **44**, 419–440.
144 A. L. Kholodenko and J. F. Douglas, *Phys. Rev. E: Stat. Phys., Plasmas, Fluids, Relat. Interdiscip. Top.*, 1995, **51**, 1081.
145 J. T. Edward, *J. Chem. Educ.*, 1970, **47**, 261.
146 A. Tuteja, M. E. Mackay, C. J. Hawker and B. Van Horn, *Macromolecules*, 2005, **38**, 8000–8011.
147 S. Jain, J. G. P. Goossens, G. W. Peters, M. van Duin and P. J. Lemstra, *Soft Matter*, 2008, **4**, 1848–1854.
148 J. Midya, M. Rubinstein, S. K. Kumar and A. Nikoubashman, *ACS Nano*, 2020, **14**, 15505–15516.
149 J. F. Pressly, R. A. Riggleman and K. I. Winey, *Macromolecules*, 2019, **52**, 6116–6125.
150 A. C. Zhang, K. Ohno and R. J. Composto, *Macromolecules*, 2024, **57**, 6634–6645.
151 Z. Yang, X. Xu, J. F. Douglas and W.-S. Xu, *J. Chem. Phys.*, 2024, **160**, 044503.
152 A. Nikoubashman, *J. Chem. Phys.*, 2021, **154**(9), 090901.
153 G. Catalini, N. A. Garca, D. A. Vega and A. Nikoubashman, *Macromolecules*, 2024, **57**, 2530–2538.
154 N. H. Nemati, K. R. Moghadam and N. Afra, *Polymer Nanocomposite Films and Coatings*, Elsevier, 2024, pp. 71–101.
155 S. Devasahayam and C. M. Hussain, *Sustainable Mater. Technol.*, 2020, **26**, e00233.
156 L.-H. Cai, S. Panyukov and M. Rubinstein, *Macromolecules*, 2011, **44**, 7853–7863.
157 T. Kataoka, T. Kitano, M. Sasahara and K. Nishijima, *Rheol. Acta*, 1978, **17**, 149–155.
158 C. Ye, C. G. Wiener, M. Tyagi, D. Uhrig, S. V. Orski, C. L. Soles, B. D. Vogt and D. S. Simmons, *Macromolecules*, 2015, **48**, 801–808.
159 N. Begam, N. Das, S. Chandran, M. Ibrahim, V. Padmanabhan, M. Sprung and J. K. Basu, *Soft Matter*, 2018, **14**, 8853–8859.
160 S. Srivastava and J. K. Basu, *Phys. Rev. Lett.*, 2007, **98**, 165701.
161 A. Sanz, H. C. Wong, A. J. Nedoma, J. F. Douglas and J. T. Cabral, *Polymer*, 2015, **68**, 47–56.
162 Z. Ma, H. Nie, J. Yan and O. K. Tsui, *J. Chem. Phys.*, 2023, **159**, 224905.
163 C. A. Angell, *J. Non-Cryst. Solids*, 1985, **73**, 1–17.
164 R. Böhmer, K. L. Ngai, C. A. Angell and D. J. Plazek, *J. Chem. Phys.*, 1993, **99**, 4201–4209.
165 S. Cheng, S.-J. Xie, J.-M. Y. Carrillo, B. Carroll, H. Martin, P.-F. Cao, M. D. Dadmun, B. G. Sumpter, V. N. Novikov and K. S. Schweizer, *et al.*, *ACS Nano*, 2017, **11**, 752–759.
166 S. Askar, L. Li and J. M. Torkelson, *Macromolecules*, 2017, **50**, 1589–1598.
167 B. A. P. Betancourt, J. F. Douglas and F. W. Starr, *Soft Matter*, 2013, **9**, 241–254.
168 M. J. Burroughs, S. Napolitano, D. Cangialosi and R. D. Priestley, *Macromolecules*, 2016, **49**, 4647–4655.
169 N. G. Perez-de Eulate, M. Sferrazza, D. Cangialosi and S. Napolitano, *ACS Macro Lett.*, 2017, **6**, 354–358.
170 N. McCrum, *Dale J. Meier, Gorden and Bread Sci*, Publisher, New York, 1978.
171 T. Kanaya, T. Kawaguchi and K. Kaji, *J. Chem. Phys.*, 1996, **104**, 3841–3850.
172 J. Colmenero, A. Arbe, A. Alegria, M. Monkenbusch and D. Richter, *J. Phys.: Condens. Matter*, 1999, **11**, A363.
173 A. Arbe, J. Colmenero, M. Monkenbusch and D. Richter, *Phys. Rev. Lett.*, 1998, **81**, 590.
174 E. Fischer, E. Donth and W. Steffen, *Phys. Rev. Lett.*, 1992, **68**, 2344.
175 M. Jhalaria, E. Buenning, Y. Huang, M. Tyagi, R. Zorn, M. Zamponi, V. Garca-Sakai, J. Jestin, B. C. Benicewicz and S. K. Kumar, *Phys. Rev. Lett.*, 2019, **123**, 158003.
176 J. Colmenero, F. Alvarez and A. Arbe, *Phys. Rev. E: Stat., Nonlinear, Soft Matter Phys.*, 2002, **65**, 041804.

177 A. Arbe, J. Colmenero, F. Alvarez, M. Monkenbusch, D. Richter, B. Farago and B. Frick, *Phys. Rev. Lett.*, 2002, **89**, 245701.
178 J. Zhao, Y. H. Chin, Y. Liu, A. A. Jones, P. T. Inglefield, R. P. Kambour and D. M. White, *Macromolecules*, 1995, **28**, 3881–3889.
179 C. M. Roland and R. Casalini, *J. Chem. Phys.*, 2003, **119**, 1838–1842.
180 A. Narros, A. Arbe, F. Alvarez, J. Colmenero and D. Richter, *J. Chem. Phys.*, 2008, **128**, 224905.
181 A.-C. Genix, A. Arbe, F. Alvarez, J. Colmenero, B. Farago, A. Wischnewski and D. Richter, *Macromolecules*, 2006, **39**, 6260–6272.
182 G. P. Kar, N. Begam, J. K. Basu and S. Bose, *Macromolecules*, 2014, **47**, 7525–7532.
183 S. Srivastava, J. L. Schaefer, Z. Yang, Z. Tu and L. A. Archer, *Adv. Mater.*, 2014, **26**, 201–234.
184 H. Chao, B. A. Hagberg and R. A. Riggleman, *Soft Matter*, 2014, **10**, 8083–8094.
185 M. Segev-Bar and H. Haick, *ACS Nano*, 2013, **7**, 8366–8378.
186 P. Kanjanaboos, X.-M. Lin, J. E. Sader, S. M. Rupich, H. M. Jaeger and J. R. Guest, *Nano Lett.*, 2013, **13**, 2158–2162.
187 J. A. Rogers, T. Someya and Y. Huang, *Science*, 2010, **327**, 1603–1607.
188 K. E. Mueggenburg, X.-M. Lin, R. H. Goldsmith and H. M. Jaeger, *Nat. Mater.*, 2007, **6**, 656–660.
189 C. R. Bilchak, E. Buenning, M. Asai, K. Zhang, C. J. Durning, S. K. Kumar, Y. Huang, B. C. Benicewicz, D. W. Gidley and S. Cheng, *et al.*, *Macromolecules*, 2017, **50**, 7111–7120.
190 J. He, X.-M. Lin, H. Chan, L. Vukovic, P. Král and H. M. Jaeger, *Nano Lett.*, 2011, **11**, 2430–2435.
191 H. B. Park, J. Kamcev, L. M. Robeson, M. Elimelech and B. D. Freeman, *Science*, 2017, **356**, eaab0530.
192 C. K. Sarika, G. Tomar, J. K. Basu and U. Thiele, *Soft Matter*, 2015, **11**, 8975–8980.
193 S. Markutsya, C. Jiang, Y. Pikus and V. V. Tsukruk, *Adv. Funct. Mater.*, 2005, **15**, 771–780.
194 R. Hou, C. Fong, B. D. Freeman, M. R. Hill and Z. Xie, *Sep. Purif. Technol.*, 2022, **300**, 121863.
195 X. Lu, W. Zhang, C. Wang, T.-C. Wen and Y. Wei, *Prog. Polym. Sci.*, 2011, **36**, 671–712.
196 S. Shen, Y.-C. Dong, W. K. Ng, L. Chia and R. Tan, *Nanotechnologies for the life sciences*, 2010.
197 R. De, M. K. Mahata and K.-T. Kim, *Adv. Sci.*, 2022, **9**, 2105373.
198 L. F. Greenlee, D. F. Lawler, B. D. Freeman, B. Marrot and P. Moulin, *Water Res.*, 2009, **43**, 2317–2348.
199 G. M. Geise, H. B. Park, A. C. Sagle, B. D. Freeman and J. E. McGrath, *J. Membr. Sci.*, 2011, **369**, 130–138.
200 R. W. Baker, *Membrane technology and applications*, John Wiley & Sons, 2023.
201 M. Mulder, *Basic principles of membrane technology*, Springer science & business media, 2012.
202 C. Nagel, K. Günther-Schade, D. Fritsch, T. Strunskus and F. Faupel, *Macromolecules*, 2002, **35**, 2071–2077.
203 S. C. George and S. Thomas, *Prog. Polym. Sci.*, 2001, **26**, 985–1017.
204 H. Lin, E. Van Wagner, B. D. Freeman, L. G. Toy and R. P. Gupta, *Science*, 2006, **311**, 639–642.
205 H. B. Park, C. H. Jung, Y. M. Lee, A. J. Hill, S. J. Pas, S. T. Mudie, E. Van Wagner, B. D. Freeman and D. J. Cookson, *Science*, 2007, **318**, 254–258.
206 C. R. Bilchak, M. Jhalaria, Y. Huang, Z. Abbas, J. Midya, F. M. Benedetti, D. Parisi, W. Egger, M. Dickmann and M. Minelli, *et al.*, *ACS Nano*, 2020, **14**, 17174–17183.
207 J. W. Barnett and S. K. Kumar, *Soft Matter*, 2019, **15**, 424–432.
208 M. Jhalaria, Y. Huang, E. Ruzicka, M. Tyagi, R. Zorn, M. Zamponi, V. Garca Sakai, B. Benicewicz and S. Kumar, *Macromolecules*, 2021, **54**, 6968–6974.
209 C. R. Bilchak, M. Jhalaria, S. Adhikari, J. Midya, Y. Huang, Z. Abbas, A. Nikoubashman, B. C. Benicewicz, M. Rubinstein and S. K. Kumar, *Macromolecules*, 2022, **55**, 3011–3019.
210 L. M. Robeson, *J. Membr. Sci.*, 1991, **62**, 165–185.
211 S. Chandran, J. Baschnagel, D. Cangialosi, K. Fukao, E. Glynos, L. M. Janssen, M. Müller, M. Muthukumar, U. Steiner and J. Xu, *et al.*, *Macromolecules*, 2019, **52**, 7146–7156.
212 S. Chandran and G. Reiter, *Macromolecular Engineering: From Precise Synthesis to Macroscopic Materials and Applications*, 2022, pp. 1–30.
213 M. Müller, *Prog. Polym. Sci.*, 2020, **101**, 101198.

